

PROBING THE EXTENT OF VERTICAL MIXING IN BROWN DWARF ATMOSPHERES WITH DISEQUILIBRIUM CHEMISTRY

SAGNICK MUKHERJEE¹ , JONATHAN J. FORTNEY¹ , NATASHA E. BATALHA² , THEODORA KARALIDI³ , MARK S. MARLEY⁴ , CHANNON VISSCHER⁵ , BRITTANY E. MILES¹ , AND ANDREW J. I. SKEMER¹ 

¹Department of Astronomy and Astrophysics, University of California, Santa Cruz, CA 95064, USA

²NASA Ames Research Center, MS 245-3, Moffett Field, CA 94035, USA

³Department of Physics, University of Central Florida, 4111 Libra Dr, Orlando, FL 32816, USA

⁴Lunar and Planetary Laboratory, The University of Arizona, Tucson, AZ 85721, USA

⁵Dordt University, Sioux Center IA; Space Science Institute, Boulder, CO, USA

Draft version August 31, 2022

ABSTRACT

Evidence of disequilibrium chemistry due to vertical mixing in the atmospheres of many T and Y-dwarfs has been inferred due to enhanced mixing ratios of CO and reduced NH₃. Atmospheric models of planets and brown dwarfs typically parameterize this vertical mixing phenomenon with the vertical eddy diffusion coefficient, K_{zz} . While K_{zz} can perhaps be approximated in the convective regions in the atmosphere with mixing length theory, in radiative regions the strength of vertical mixing is uncertain by many orders of magnitude. With a new grid of self-consistent 1D model atmospheres from T_{eff} of 400 - 1000 K, computed with a new radiative-convective equilibrium python code PICASO 3.0, we aim to assess how molecular abundances and corresponding spectra can be used as a probe of depth-dependent K_{zz} . At a given surface gravity, we find non-monotonic behavior in the CO abundance as a function of T_{eff} , as chemical abundances are sometimes quenched in either of two potential atmospheric convective zones, or quenched in either of two possible radiative zones. The temperature structure and chemical quenching behavior also changes with gravity. We compare our models with available near-infrared and M-band spectroscopy of several T and Y-dwarfs and assess their atmospheric vertical mixing profiles. We also compare to color-magnitude diagrams and make predictions for JWST spectra. This work yields new constraints, and points the way to significant future gains, in determining K_{zz} , a fundamental atmospheric parameter in substellar atmospheres, with significant implications for chemistry and cloud modeling.

Keywords: Brown Dwarfs, T dwarfs, Y dwarfs, Atmospheric Composition

1. INTRODUCTION

1.1. *Molecular abundances and non-equilibrium chemistry*

The astronomical community is now ready to observe the atmospheres of a diverse range of exoplanets and brown dwarfs in unprecedented detail with the *James Webb Space Telescope* (JWST) (Gardner et al. 2006; Pontoppidan et al. 2022). These atmospheres are complex systems with a range of physical processes like radiative/convective energy transport, chemical reaction networks, clouds/haze formation, and dynamical processes like vertical mixing. Upcoming high signal-to-noise (SNR) spectra from JWST for these substellar atmospheres will provide us with a unique opportunity to probe these physical and chemical processes and compare to state-of-the-art theoretical models. Therefore, it is crucial to develop and update these models by including necessary complex processes and assessing how uncertainties in physical and chemical parameters affect the structure, abundances, and spectra of these atmospheres.

One such complex process in substellar atmospheres is atmospheric dynamics. Dynamics is a three-dimensional process. In the case of solar system planets, atmospheric

dynamics can be directly studied with spatially and time resolved imaging or spectroscopy. Although, we cannot spatially resolve brown dwarfs and exoplanets, dynamical processes can still be studied by their impact on molecular abundances and condensate clouds, which affect their spectra and lightcurves. Surface inhomogeneities can be probed via rotationally modulate lightcurves (Metchev et al. 2015; Cushing et al. 2016; Karalidi et al. 2015; Vos et al. 2022), often in two dimensions when observed at a single wavelength. Spectra, which probe a range of atmospheric pressures, provide a potential view of dynamics in the additional dimension of atmosphere depth. Processes like convection, the breaking of gravity waves, and convective overshoot can impact both the chemical and cloud structure of these atmospheres by causing net vertical transport of atmospheric gases and particles across many atmospheric scale heights (Freytag et al. 2010; Parmentier et al. 2013; Bordwell et al. 2018; Tan 2022).

Dynamical processes can also alter the abundances of atmospheric gases in the visible atmosphere by transporting gas molecules through several scale heights, on a timescale faster than chemical reactions are able to locally equilibrate to their new surroundings. This leads to departures from the chemical equilibrium, often assumed as a starting point in exoplanet and brown dwarf atmosphere models (e.g., Marley et al. 2021). The dynamics induced transport of gases and particles along the radial

dimension of these atmospheres is called “vertical mixing”. Vertical mixing can lead to disequilibrium chemical abundances in substellar atmospheres for gases like CO, CH₄, H₂O, NH₃, CO₂, PH₃, and HCN (Fortney et al. 2020; Tsai et al. 2017, 2021; Moses et al. 2011). Because most of these gases are major sources of opacities in substellar atmospheres (H₂O, CH₄, CO, etc.), their spectra can be altered significantly.

Vertical mixing also directly affects cloud formation through its effect on molecules like H₂O in Y-dwarfs and colder exoplanets (Morley et al. 2014; Ackerman & Marley 2001a; Gao et al. 2020). Vertical mixing transports condensable vapor from the deeper atmosphere to lower pressures and temperatures, where they condense. Moreover, mixing counteracts gravitational settling, and therefore helps to dictate the size of cloud particles that can remain aloft. As a result, the atmospheric vertical mixing significantly impacts the cloud opacity by controlling the cloud vertical extent and particle size distribution. As both the chemical and cloud structure of these atmospheres impact radiative and convective energy transport, vertical mixing also affects the temperature structure of substellar atmospheres.

There is already decades-deep literature on observations and modeling of disequilibrium chemistry in Jupiter and Saturn (Beer 1975; Larson et al. 1978; Prinn & Barshay 1977; Larson et al. 1977; Fegley & Prinn 1985; Visscher et al. 2010b), and in T-dwarfs and early Y-dwarfs (Fegley & Lodders 1996; Noll et al. 1997; Oppenheimer et al. 1998; Saumon et al. 2003; Golimowski et al. 2004; Hubeny & Burrows 2007; Geballe et al. 2009; Sorahana & Yamamura 2012; Leggett et al. 2012; Visscher et al. 2010a; Visscher & Moses 2011; Zahnle & Marley 2014; Miles et al. 2020). We briefly summarize the key developments in the field in §1.2. But, more recently, Miles et al. (2020) obtained M-band spectra of four late T and early Y-dwarfs and used archival M-band spectra of two T-dwarfs and a Y-dwarf to infer the strength of vertical mixing in their atmospheres as a function of T_{eff} . They determined the CO abundance in each of these objects by fitting models to spectra. 1D brown dwarf atmospheric models with equilibrium chemistry were post-processed to include the effect of disequilibrium chemistry due to vertical mixing to interpret the observed CO abundances and infer the vigor of vertical mixing in these atmospheres. This demonstrated that measurements of chemical abundances of various gases along with 1D forward models can be used to constrain vertical mixing in substellar atmospheres. However, disequilibrium chemistry can lead to significant changes in the atmospheric state of these objects compared to equilibrium chemistry calculations due to the feedback of the modified chemical abundances of gases on the atmospheric temperature structure (Hubeny & Burrows 2007; Karalidi et al. 2021; Phillips et al. 2020).

The Miles et al. (2020) paper and new modeling work points to the possibility of using upcoming high SNR JWST spectra of brown dwarfs to probe their atmospheric structure and atmospheric chemistry in a much more detailed way. The rationale of our study here is to specifically examine how differences in the strength of vertical mixing, and how it is typically parametrized in convective and radiative atmospheric regions, gives rise to distinct differences in model spectra. Comparison

with measured spectra now and in the future can then be used to assess the mixing speed in convective and radiative regions, yielding novel constraints on atmospheric physics.

1.2. Modeling Approaches

Mixing in substellar atmospheres is a 3-dimensional process. Both 2D and 3D models have been used to study vertical mixing in hotter brown dwarfs and hot Jupiters (Tan 2022; Tan & Showman 2021; Parmentier et al. 2013; Freytag et al. 2010; Bordwell et al. 2018). However, a full exploration of the relevant parameter space of brown dwarf mixing properties, is currently not feasible with 3D models. Moreover, these 3D models often include simplified or gray radiative transfer, so in detail the calculated temperature structures yield model spectra that are not yet an adequate match to measured spectra (Tan & Showman 2021; Mukherjee et al. 2021). Chemical equilibrium is also often assumed in GCMs (e.g., Lee et al. 2021; Showman et al. 2009) but some models also treat chemical species within a passive transport framework (e.g., Parmentier et al. 2013; Komacek et al. 2019; Tan 2022) to explore the effects of atmospheric mixing on chemical structure of substellar atmospheres.

1D self-consistent models, which iterate to a radiative-convective equilibrium (RCE) solution, given specified atmospheric physics and chemistry, include many of the complex physical processes of real atmospheres and can be used to produce high SNR model observables. Given the relatively fast computational times, they are important in exploring wide ranges of parameter space (e.g. Marley et al. 1996; Burrows et al. 1997; Marley & McKay 1999; Burrows et al. 2003; Fortney et al. 2008; Morley et al. 2014; Gandhi & Madhusudhan 2017; Malik et al. 2017; Marley et al. 2021). Although such models only include one dimension, the effects of dynamics can still be included. This is typically done by approximating vertical mixing as a diffusive process, and parameterizing this diffusive “speed” with a single vertical eddy diffusion coefficient – K_{zz} (Allen et al. 1981) which has dimensions of $[L]^2/[T]$, where $[L]$ and $[T]$ represent length and time, respectively. However, theoretical and observational constraints of K_{zz} , and its dependence on temperature and pressure, is uncertain by several orders of magnitude today (Fortney et al. 2020; Miles et al. 2020; Phillips et al. 2020).

The vigor of vertical mixing could well have a complex behavior, even within the atmosphere of a single object. Brown dwarf atmospheres have convective and radiative zones. In the convective zones mixing is expected to be comparatively efficient with higher values of K_{zz} , compared to the radiative zones which are stable to convection. Theoretically, K_{zz} has been approximated with mixing length theory in the convective zones of these atmospheres (e.g., Ackerman & Marley 2001b; Smith 1998; Gierasch & Conrath 1985). However, this approximation is still uncertain due to uncertainties in key parameters in the mixing length theory like the mixing length itself. Theoretical understanding of K_{zz} is even more primitive in the case of radiative zones. Typically, K_{zz} is varied by a factor of a *million* or more, with its effects on the temperature structure and atmospheric abundances inadequately explored. This poor knowledge of K_{zz} leaves large gaps in our understanding of vertical mixing on

chemistry, clouds, and temperature structure.

Previously, several authors computed RCE models that treated non-equilibrium chemical abundances self-consistently with the atmospheric temperature structure (e.g. Hubeny & Burrows 2007; Phillips et al. 2020; Karalidi et al. 2021). However, these models were all computed either within the framework of a constant K_{zz} value in the atmosphere, with an exploration of K_{zz} varied across many orders of magnitude (e.g. Karalidi et al. 2021; Phillips et al. 2020), or with K_{zz} computed using mixing length theory in the convective zones and constant K_{zz} in the radiative zones (e.g. Hubeny & Burrows 2007). We build on these works, but aim for a more precise assessment of how a changing K_{zz} within a given atmosphere, due to convective- and radiative-zone mixing, alters atmospheric abundances and spectra. The output from 3D GCMs show that K_{zz} can vary by several orders of magnitude with pressure in a substellar atmosphere (Freytag et al. 2010; Parmentier et al. 2013; Tan 2022), but this has not yet been implemented within a self-consistent RCE model.

Observations from Miles et al. (2020) showed that T-dwarfs with T_{eff} between 400–800 K have much smaller K_{zz} than expected from convective mixing. They also found a factor of 100 *increase* in the inferred K_{zz} in these brown dwarfs when T_{eff} *decreased* below ~ 400 K. Miles et al. (2020) suggested an explanation for this behavior if in the warm objects with T_{eff} between 400–800 K, gases are “quenched” within a radiative part of the atmosphere (lower K_{zz}), but in a convective part of the atmosphere in objects with $T_{\text{eff}} < 400$ K. Therefore, already available observations demand models with higher complexity than a constant K_{zz} approach. This is especially needed to prepare these models adequately to interpret the much higher quality data expected from JWST.

In this work, we enhance the models presented in Karalidi et al. (2021) by inclusion of temperature- and pressure- dependant K_{zz} profiles within the 1D RCE framework. We use this model to explore the complex interconnections between K_{zz} , the temperature structure, molecular abundances, and spectra in late T and early Y-dwarfs. We use this model and already available ground-based spectroscopic data of six brown dwarfs to address the following questions,

1. How does a self-consistent treatment of vertical mixing affect the $T(P)$ profile?
2. Does a self-consistent treatment of K_{zz} cause changes in the radiative and convective zone locations and depths in brown dwarfs compared to equilibrium chemistry models?
3. In what objects can we expect quenching of gases like CO, CH₄ and NH₃ to occur in radiative zones instead of convective zones?
4. Is photometry and spectroscopy of brown dwarfs between 1–14 μm sensitive to the K_{zz} in the radiative and convective zone?
5. How much can we learn about the atmospheric properties of late T-dwarfs by applying self-consistent disequilibrium chemistry models on already available infrared spectral data?

6. Can JWST be used to accurately infer the vertical mixing strength in radiative zones and convective zones of brown dwarfs?

We briefly discuss our new Python based atmospheric model in §2. We present our results in §3 followed by discussion of our results in §4 and conclude in §5

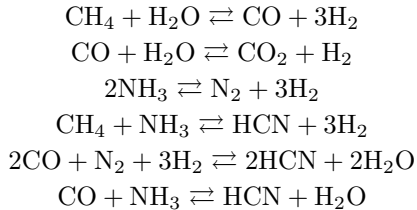
2. MODELING SUB-STELLAR ATMOSPHERES

We have adapted the Fortran based EGP sub-stellar atmospheric model to Python. This new Python version of the EGP code is open-source and available as a part of the widely used Python exoplanet atmospheric modeling tool PICASO (Batalha et al. 2019), as a part of the PICASO 3.0 (Mukherjee et al. 2022) release. The numerical and functional details of the code along with a series of benchmarks with previously available models are presented in Mukherjee et al. (2022). The EGP model has been used by our group for substellar atmospheres for over two decades (Marley et al. 1996; Marley et al. 2012; Fortney et al. 2005, 2007, 2008; Morley et al. 2014; Marley et al. 2021; Karalidi et al. 2021). Recently, Karalidi et al. (2021) updated the Fortran based EGP code with the capability to include constant K_{zz} and its impact on chemistry self-consistently. We have converted this version of the code in Python and have modified it by including the capability to treat pressure-dependent variable K_{zz} in substellar atmospheres. Here we briefly describe the model methodology used in this work and we refer the reader to Mukherjee et al. (2022) for a more detailed discussion of the numerical methodology of our models.

2.1. Python Based implementation of EGP with Disequilibrium Chemistry

We divide the 1D model atmosphere in 90 pressure layers (91 layer boundaries or levels) with logarithmically-spaced pressure values. From an initial guess temperature-pressure ($T(P)$) profile, the model iterates on the $T(P)$ profile, atmospheric chemistry, and radiative/convective energy transport using a Newton-Raphson method, yielding temperature corrections at each pressure level. These iterations continue until it finds the converged atmospheric state in which radiative-convective equilibrium is satisfied throughout the atmosphere. Self-consistent modeling of effects like disequilibrium chemistry due to vertical mixing requires simultaneous calculation of gas abundances and opacities with the iteration on the $T(P)$ profile instead of interpolation on a precomputed grid.

Each chemical reaction in the atmosphere proceeds with a characteristic timescale t_{chem} which is a strong function of temperature, pressure, and the chemical composition of the atmosphere. Zahnle & Marley (2014) used 1D chemical kinetics models to parameterize t_{chem} expression for the major O-, C-, H-, and N-bearing reactions in substellar atmospheres. These reactions often are a part of a large network of chemical reactions with many chemical species but still can be represented by simpler net reactions between a few species of interest. The net chemical reactions between O-, C-, H- and N-bearing gases we consider here are,



Vertical mixing in the atmosphere also proceeds with a typical timescale, which is associated with the eddy diffusion coefficient K_{zz} ,

$$t_{\text{mix}} = \frac{H^2}{K_{zz}} \quad (1)$$

where H is the local scale height of that atmospheric layer. t_{chem} is generally much shorter than t_{mix} in high pressure, high temperature regions of the atmosphere where gas abundances are expected to follow chemical equilibrium. But as the atmosphere gets colder at lower pressures t_{chem} rises exponentially and becomes much longer than t_{mix} . The pressure at which the intersection between the two timescales occurs is called the “quench pressure” or “quench level.” At all pressure levels lower than the quench pressure (higher up the atmosphere) atmospheric abundances for the relevant chemical compounds take on the abundances at the relevant quench pressure, rather than those of equilibrium chemistry at the local P and T . In the brown dwarf context this behavior was first predicted by [Fegley & Lodders \(1996\)](#) and observed by [Noll et al. \(1997\)](#).

Within our model, the $T(P)$ profile is used to calculate the K_{zz} as a function of each model layer’s pressure. K_{zz} in the convective zone is calculated with mixing length theory ([Gierasch & Conrath 1985](#)),

$$K_{zz} = \frac{H}{3} \left(\frac{L}{H} \right)^{4/3} \left(\frac{RF}{\mu\rho_a c_p} \right)^{1/3} \quad (2)$$

where H is the local scale height of the atmosphere, L is the turbulent mixing length, R is the universal gas constant, μ is the mean molecular weight of the atmosphere, ρ_a is the atmospheric density, c_p is the atmospheric specific heat at constant pressure and F is the convective heat flux. The convective heat flux is given by the difference between σT_{eff}^4 and the radiative flux at each layer within the convective zones of the atmosphere. The maximum convective heat flux would then be σT_{eff}^4 . Here the convective heat flux is calculated self-consistently in each layer. The turbulent mixing length L is set to be equal to the scale height (H) in our models. But in order to explore scenarios where convective mixing is less effective, we also simulate cases where the mixing length is smaller than the atmospheric scale height H by a factor of 10. Note that this turbulent mixing length (L) was only changed in Equation 2 and not in Equation 1. The mixing length in Equation 1 remained the same as the local atmospheric scale height throughout this study. For further background, we refer the reader to previous work (e.g. [Visscher & Moses 2011](#); [Smith 1998](#); [Bordwell et al. 2018](#); [Bézard et al. 2002](#); [Visscher et al. 2010b](#)) ex-

ploring the relationship between mixing length and the scale height in Equation 1.

Over the past several years various parameterizations of K_{zz} in the radiative zones of substellar atmospheres have been discussed in the literature (e.g., [Wang et al. 2015](#); [Zhang & Showman 2018](#); [Parmentier et al. 2013](#)). As a starting point, we use the parametrization from [Moses et al. \(2021\)](#),

$$K_{zz} = \frac{5 \times 10^8}{\sqrt{P_{\text{bar}}}} \left(\frac{H_{1\text{mbar}}}{620 \text{ km}} \right) \left(\frac{T_{\text{eff}}}{1450 \text{ K}} \right)^4 \quad (3)$$

where P_{bar} is the pressure in bars and $H_{1\text{mbar}}$ is the atmospheric scale height at 10^{-3} bars. The $5 \times 10^8 / \sqrt{P}$ dependence was estimated by [Parmentier et al. \(2013\)](#) using tracer transport in 3D GCM for hot Jupiter HD209458b. This dependence was found to be valid for this object between 10^{-6} -1 bars. The $P^{-0.5}$ dependence captures the increase of K_{zz} with lowering pressure in the radiative zone as mixing can be efficient in low pressure ($P \sim 10^{-4}$ bars) parts of the radiative atmosphere due to mechanisms like gravity wave breaking ([Freytag et al. 2010](#)). The factor $H_{1\text{mbar}} T_{\text{eff}}^4$ was also included in the parametrization as this factor shows good correlation with the measured K_{zz} (via photochemical models) of solar system planets (including Jupiter, Saturn, Uranus, Neptune, Earth, and Venus) and exoplanets ([Moses et al. 2005](#); [Zhang & Showman 2018](#); [Moses et al. 2021](#)). But, as the $T(P)$ structure of brown dwarfs can be quite different from irradiated planets, we also explore deviations from this parametrization where this relation is increased or decreased by factors of 100 to explore the relevant parameter space. As the $T(P)$ profile iterates towards the converged solution, the K_{zz} in convective zones, given by Equation 2 and the K_{zz} in radiative zones, given by Equation 3, evolve as well. The mixing timescale in each atmospheric layer is then calculated in every iteration from this K_{zz} using Equation 1. The quench pressures of each of these chemical species are found by comparing t_{mix} with t_{chem} expressions from [Zahnle & Marley \(2014\)](#). The abundances of CO, CH₄, NH₃, CO₂, H₂O and HCN are allowed to follow equilibrium chemistry at pressures higher than their relevant “quench pressure” and their abundances are quenched above the quench pressure level. But as the $T(P)$ profile iterates to the converged solution, the quench pressure of various gases also change at each step as both the t_{chem} and t_{mix} are dependent on the $T(P)$ profile of the atmosphere. This requires the RCE model to include “on-the-fly” calculations of both chemistry and opacities in order to include disequilibrium chemistry self-consistently in the calculations.

As in [Karlidi et al. \(2021\)](#) we use the “on-the-fly mixing” method of opacities following the methodology of [Amundsen et al. \(2017\)](#). In this work we focus on the quenching of CO, CH₄, H₂O, NH₃, N₂, HCN and PH₃. Of these, only CO, CH₄, H₂O, and NH₃ are major opacity sources. Therefore, we mix the correlated-k opacities of CO, CH₄, H₂O, and NH₃ with the correlated-k opacities of all the other sets of gases which follow equilibrium chemistry as the volume mixing ratio of these gases evolve due to quenching with the $T(P)$ profile of the atmosphere. As in [Karlidi et al. \(2021\)](#), given inac-

curacies inherent in the flexible Amundsen et al. (2017) resort-rebin approach necessitates the use of a denser grid of 661 wavelength bins, compared to the 196 used for our equilibrium chemistry models (Marley et al. 2021).

We benchmark the code in two ways: 1) by setting $K_{zz}=0$ and finding that the on-the-fly mixing method still converges to the equilibrium chemistry solutions from Marley et al. (2021), and 2) by testing the resulting models against results obtained by Phillips et al. (2020) with non-zero but constant K_{zz} values. The benchmarking results are presented in Mukherjee et al. (2022). The code results matches well with both models. In future work the code will be further enhanced via coupling with 1D chemical kinetics model VULCAN (Tsai et al. 2017, 2021) so that it can self-consistently treat both vertical mixing and photochemistry. This Python based code will be open-sourced as a part of the PICASO 3.0 package. Next, we discuss results obtained by applying this code to model disequilibrium chemistry and characterize mixing strengths in late T and early Y-dwarf atmospheres.

3. RESULTS

We performed a detailed four dimensional parameter space exploration of how varied vigor of vertical mixing in brown dwarf atmospheres affects the atmospheric state and spectra. We produced a grid of models by varying four physical parameters – T_{eff} , gravity, radiative zone K_{zz} , and convective zone mixing length L . The gravity has been varied across five values 316, 562, 1000, 1780 and 3160 ms^{-2} ($\log(g)$ from 4.5 to 5.5 with an interval of 0.25 dex). The T_{eff} range is 400 K to 1000 K with an interval of 25 K.

To explore the role of radiative zone K_{zz} , in our grids we multiply Equation 3 by a multiplicative factor of $\times 100$, $\times 1$, and $\times 0.01$. We refer to these parameter values as “Moses $\times 100$ ”, “Moses”, and “Moses/100”, respectively, after Moses et al. (2021). The mixing length parameter in the convective zones (L in Equation 2) has been varied between the scale height H and $0.1 \times H$ to explore scenarios where mixing in the convective zone is less efficient than the typically assumed mixing length theory in 1D models. Furthermore, for reasons discussed in §4, we ran two sets of models – one where PH_3 is quenched given its appropriate t_{chem} and another where PH_3 follows equilibrium chemistry while other molecules are quenched. This parameter space has a total of $5 \times 25 \times 3 \times 2 \times 2 = 1500$ self-consistent radiative-convective equilibrium models. All of these models are cloud free and assume solar metallicity and C/O ratio, following Marley et al. (2021). We haven’t included clouds in our models as at the temperature range of our grid (400 – 1000 K), clouds are not expected to be a significant opacity source in the upper atmosphere. We present our key findings from this grid of models below beginning with the feedback of disequilibrium chemistry on $T(P)$ profiles of brown dwarfs.

3.1. Effect of Disequilibrium Chemistry on the $T(P)$ profile of brown dwarfs

Disequilibrium chemistry leads to enhanced CO, depleted CH_4 , NH_3 , and H_2O abundances in T and Y-dwarfs. This leads to major changes in the wavelength-dependent optical depths in the atmosphere. The top

four panels of Figure 1 shows the $\tau = 1$ pressure levels, for specific gases, for a T-dwarf with $T_{\text{eff}} = 700$ K and $\log(g) = 5.0$ in the presence and absence of quenching due to vertical mixing. These $\tau = 1$ pressure levels are strongly wavelength dependent. Here K_{zz} has been assumed to follow Equation 2 in the convective zones and Equation 3 in radiative zones. The disequilibrium chemistry pressure levels are shown in solid lines and the corresponding equilibrium chemistry levels are shown as dotted lines. The pressure-dependant volume mixing ratios of these gases under chemical equilibrium and disequilibrium are also shown in the top x-axis in each of the top four panels with dashed and solid black lines, respectively.

The bottom panels in Figure 1 depicts the log of the ratio in the $\tau = 1$ pressure level between these two models. Values greater than zero represent shallower depth probed, due to an increase in an absorber of interest, for instance CO in yellow in the third column, in particular at 4.5-5 μm . There are also significant changes due to depleted NH_3 and CH_4 . There is a more modest effect on H_2O . Overall, since major opacity sources H_2O , NH_3 , CH_4 are depleted, and they absorb across a broad wavelength range, one sees deeper, to a higher pressure, in a disequilibrium chemistry model.

A manifestation of these effects are shown in Figure 2, which shows temperature structure (upper left), CO mixing ratios (upper right), and spectra (bottom) three models at $T_{\text{eff}} = 500, 700,$ and 1000 K and $\log(g) = 5$. Solid lines include induced quenching and dashed lines represent equilibrium chemistry. The K_{zz} for these models evolved self-consistently following mixing length theory in the convective zones and followed Equation 3 in the radiative zones.

Disequilibrium abundances mainly lead to colder $T(P)$ profiles compared to equilibrium chemistry models as can be seen in Figure 2. In the overall optically thinner disequilibrium chemistry atmosphere (see Figure 1) one must see down to a higher pressure to obtain a given T . This effect was also seen in Karalidi et al. (2021) for constant K_{zz} models.

Volume mixing ratio profiles of CO for each of these models are shown in the top right panel of Figure 2. As described earlier, disequilibrium chemistry greatly enhances the CO abundances above quench level. However, even deep down, below the quench level, there are important CO abundance differences due to differences in the converged $T(P)$ profile. As equilibrium chemistry models have hotter $T(P)$ profiles, at a given pressures, than disequilibrium chemistry models, they also have higher CO abundances. This drives home the point that a self-consistent treatment of disequilibrium chemistry (as in §2.1) is needed rather than post-processing self-consistent equilibrium chemistry models with quenched abundances. Even if one obtains the correct quench pressures during post-processing equilibrium chemistry models, one would calculate a physically inconsistent and higher abundance of CO at the upper atmospheres than self-consistent disequilibrium chemistry models.

The thermal emission spectra of these models are shown in Figure 2 bottom panel. The flux from these objects were normalized by their maximum flux and are plotted from the hottest model ($T_{\text{eff}}=1000$ K) at the top to the coldest model ($T_{\text{eff}}=500$ K) at the bottom. Large

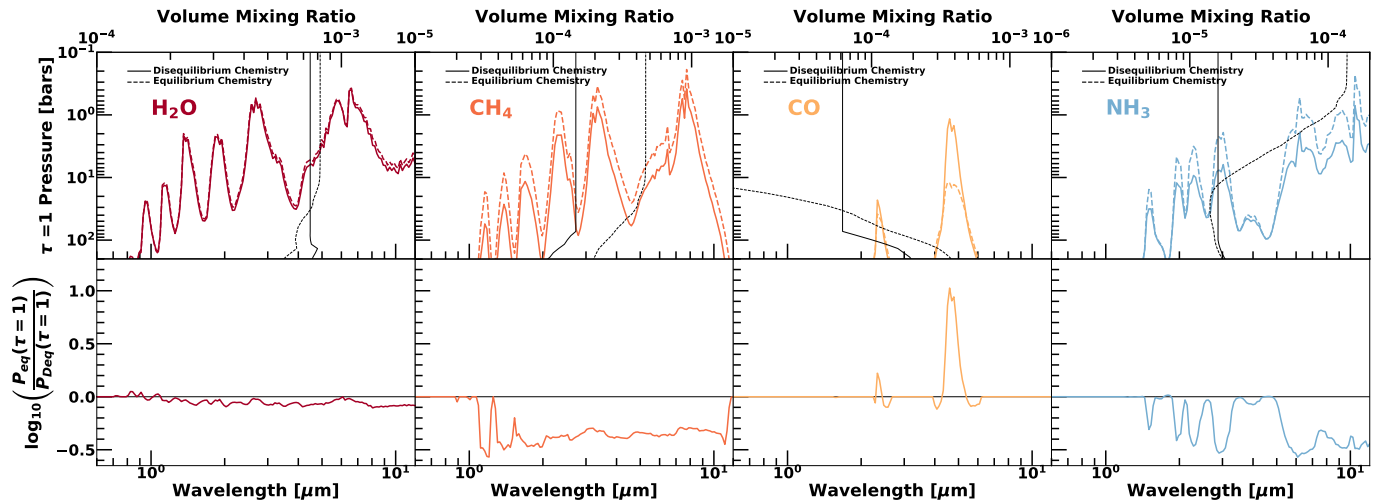


Figure 1. Top panels show the $\tau = 1$ pressure levels for specific gaseous absorbers in a model T-dwarf with $T_{\text{eff}} = 700$ K and $\log(g) = 5.0$ in the presence and absence of quenching due to vertical mixing. $\tau = 1$ pressure levels for H_2O , CH_4 , CO , and NH_3 are shown in the first, second, third and fourth columns, respectively. The equilibrium chemistry pressure levels are shown in dashed lines whereas the disequilibrium chemistry pressure levels are shown in solid lines. The volume mixing ratio as a function of pressure of each gas in the presence (solid lines) and absence (dashed lines) of vertical mixing induced quenching are also shown with black lines in the top x-axis of each of the top four panels. Bottom panels show the logarithm of the pressure ratio of these $\tau = 1$ levels with equilibrium chemistry and disequilibrium chemistry for the gaseous absorbers. The zero mark represents no change in these pressure levels. Positive values represent an increase in absorption in the disequilibrium chemistry models compared to equilibrium chemistry models. **Main Point** – Disequilibrium chemistry leads to large opacity changes in the atmosphere.

differences in outgoing thermal flux can be seen in the H, K, L and M bands between the equilibrium chemistry and disequilibrium chemistry model spectra. Comparing these differences with the differences in the $\tau = 1$ pressure levels in Figure 1 makes it clear that the differences in the H, K, and L bands arises due to changes in the CH_4 abundance profiles. Another major difference is in M-band. CO enhancement and modest H_2O depletion leads to a major suppression of thermal flux between $4.5\text{--}5\ \mu\text{m}$ in the disequilibrium models.

Although NH_3 abundances show large changes between equilibrium chemistry and disequilibrium chemistry models, it still is not the major opacity source at the shorter IR wavelengths. It becomes a major opacity source at $11\ \mu\text{m}$ and causes a distinct feature in the spectra. Figure 2 bottom panels show a significant change in this NH_3 feature due to disequilibrium chemistry. Quenching of NH_3 causes this feature to become slightly less prominent compared to chemical equilibrium models.

Other carbon and nitrogen bearing molecules like HCN , N_2 and CO_2 are also quenched due to K_{zz} . But these molecules do not have readily apparent absorption features in the infrared at these spectral resolutions in a solar metallicity mixture. N_2 is essentially transparent in solar metallicity mixtures and detecting CO_2 is very difficult from the ground but JWST, like AKARI (Sorahana & Yamamura 2012), can detect disequilibrium abundances of CO_2 in brown dwarf with higher metallicity. As our models have solar metallicity, we do not specifically discuss these signatures here.

Of particular interest to our work here are the changes in $T(P)$ structure, and the locations of radiative and convective zones show in Figure 2. We examine the causes for these differences in more detail in Figure 3 for a brown dwarf with $T_{\text{eff}} = 700$ K and $\log(g)$ of 4.5. The left panel in Figure 3 shows the $T(P)$ profile of this brown dwarf

under equilibrium chemistry with the dashed line and the $T(P)$ profile of the brown dwarf with chemical disequilibrium is shown with the solid line. The radiative zones are shown with narrower lines whereas the convective zones are shown with thicker lines.

There are significant changes in the location and number of radiative and convective zones in the two profiles, with the disequilibrium model having one convective zone at depth and radiative zone at lower pressure. However, the equilibrium models find two convective zones and two radiative zones. To examine why, the right panel in Figure 3 shows the wavelength dependent absorptivity in several layers of these atmospheres with dashed (equilibrium chemistry) and solid (disequilibrium chemistry) lines. The absorptivity is given by $A = (1 - e^{-\tau})$. A high absorptivity (close to 1) corresponds to an opaque wavelength whereas a low absorptivity corresponds to a transparent wavelength window. The normalized local blackbody Planck function B_λ is also plotted for each layer for the equilibrium (dashed black line) and disequilibrium chemistry (solid black line) models for comparison with the absorptivity. We follow Marley & Robinson (2015) for the explanation of this phenomenon below.

As the atmosphere becomes colder with lower pressure in both models, the peak of the local B_λ shifts to longer wavelengths. In the deep atmosphere ~ 100 bar, gaseous optical depths are very high which causes the absorptivity to be very close to 1 across all wavelength ranges for both cases. The atmosphere is opaque to radiative energy transport in these pressure layers for both cases, and convection ensues at these pressure levels. This is the case at pressures higher than ~ 40 bars for both models. At about 20 bars some transparent windows start to appear. Since the equilibrium chemistry model is hotter than the disequilibrium chemistry model, the peak of its local blackbody emission coincides

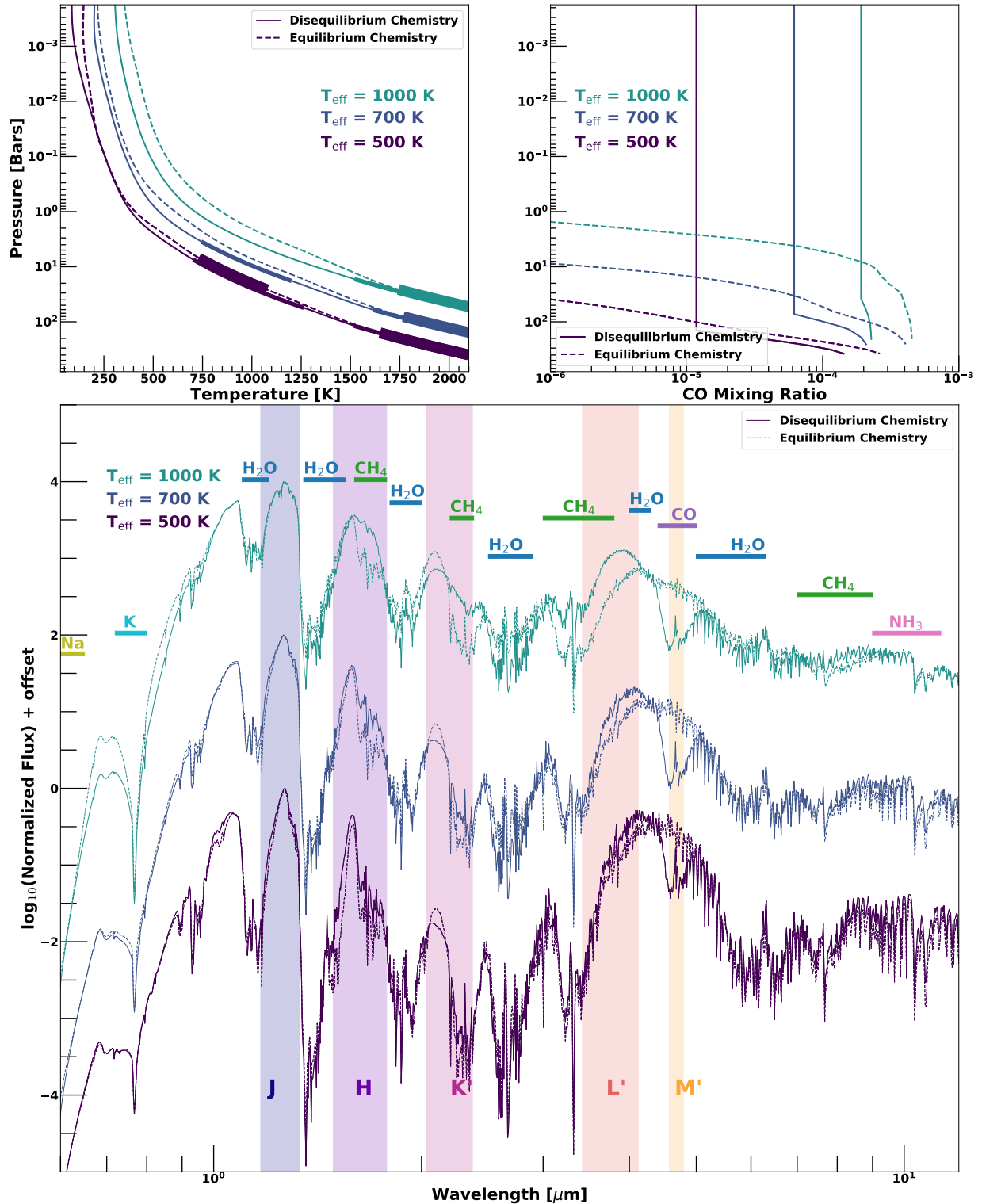


Figure 2. **Top left panel** $T(P)$ profile of brown dwarf models with $\log(g) = 5$ and T_{eff} of 500, 700, and 1000 K. The solid $T(P)$ profiles assume disequilibrium chemistry self-consistently whereas the dotted profiles show equilibrium chemistry calculations. The convective zones are shown with thicker lines for each $T(P)$ profile. To differentiate the convective zones of the equilibrium chemistry models from the disequilibrium chemistry models, they are shown with much thicker lines compared to the convective zones of disequilibrium chemistry models. **Top right panel** Plotted are the CO volume mixing ratio profiles for these brown dwarf models. The dotted lines show the mixing ratio with disequilibrium chemistry whereas the solid lines show calculations from equilibrium chemistry. **Bottom panel** shows the normalized thermal emission spectra of these brown dwarfs. The solid lines show the disequilibrium chemistry results while dotted spectra represent the equilibrium chemistry calculations. The J, H, K', L', and M' bands are also shown as shaded regions of different colors. **Main Point**– Self-consistent treatment of disequilibrium chemistry leads to large changes in $T(P)$ profile, abundances, and thermal emission spectra.

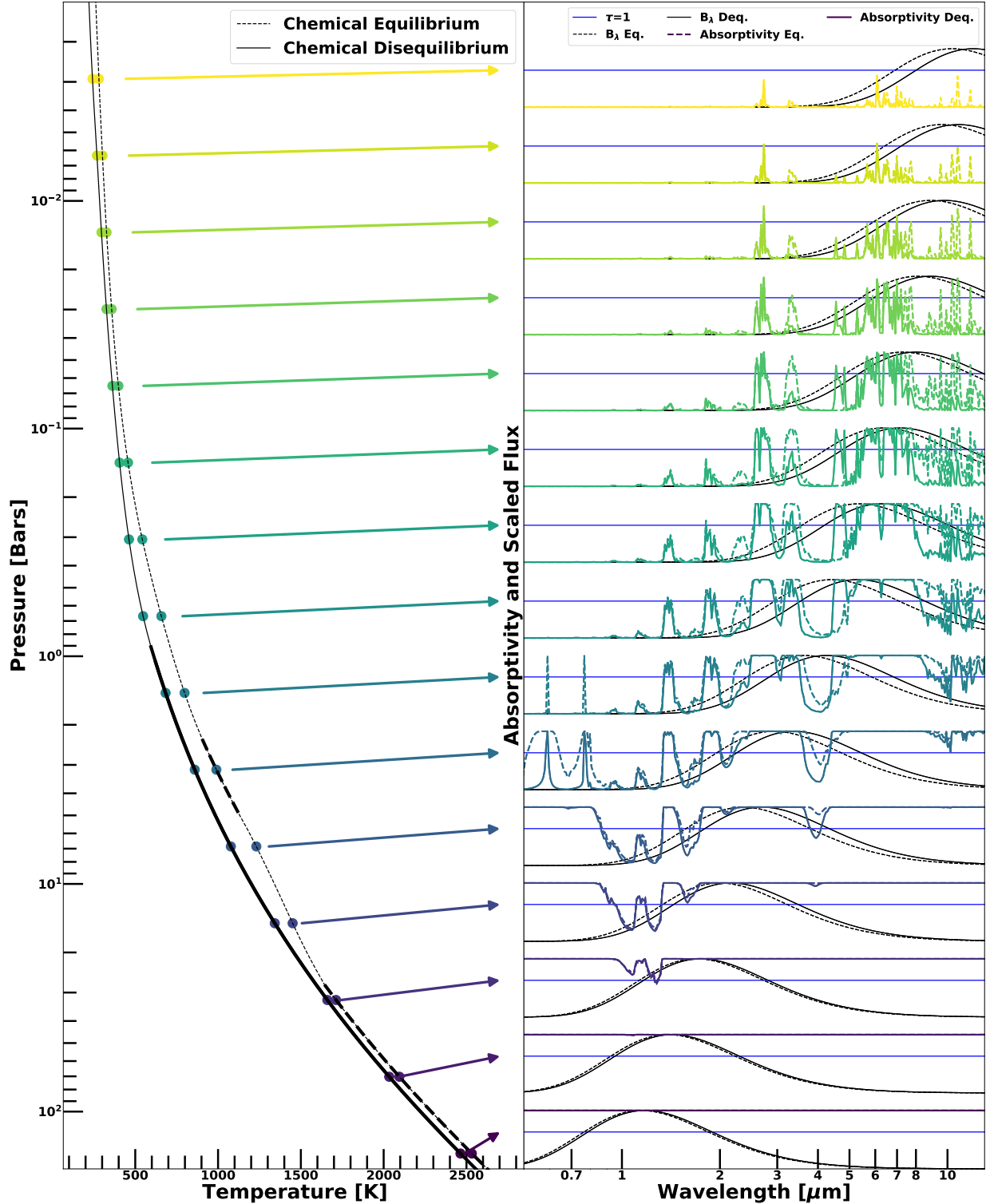


Figure 3. Left panel shows the $T(P)$ profile of a brown dwarf with T_{eff} of 700 K and $\log(g)$ of 4.5. The dashed line is the $T(P)$ profile when chemical equilibrium is assumed whereas the solid line shows the $T(P)$ profile for disequilibrium chemistry. The convective zones are shown with darker and thicker lines. Right panel shows the wavelength dependant absorptivity of the different atmospheric layers for both the cases. The absorptivity is given by $1-e^{-\tau}$. The absorptivity for the equilibrium chemistry model is shown with dashed lines whereas that for disequilibrium chemistry model are shown with solid lines. The local normalized blackbody spectrum is also shown for each layer with dashed and solid lines for equilibrium and disequilibrium chemistry models, respectively. The blue horizontal line for each layer shows the absorptivity corresponding to $\tau = 1$. **Main Point** – Opacity changes lead to large (~ 100 K) differences in $T(P)$ profiles between chemical equilibrium and disequilibrium models.

more closely in wavelength with the transparent opacity windows between 0.8-1 μm in the atmosphere at these pressures. This causes the equilibrium chemistry model to be radiative in these pressure ranges whereas the disequilibrium chemistry model is still convective as its local blackbody emission still peaks at longer wavelengths where the atmosphere is opaque at ~ 20 bars pressure. As the atmosphere gets colder with lower pressure, large transparent windows develop between 0.5-2 μm but as these layers are much colder, their blackbody peaks are at wavelengths greater than 2 μm .

At ~ 2 bars, the blackbody peak of the chemical equilibrium model hits another opaque range between 2-3 μm . This causes it to develop another, detached, convective zone at these pressures. At pressures lower than this range, a large transparent opacity window develops between 3.5-5 μm in both the models. The disequilibrium model is more transparent than the equilibrium model between 3.5-4.5 μm (due to less CH_4 and H_2O) but is more opaque than the equilibrium model between 4.5-5 μm (due to more CO). As the local blackbody function of both models also peaks between 3.5-5 μm in these pressure layers, these differences in transparency between the two atmospheres causes a large change (~ 150 K) between their $T(P)$ profiles in these pressures. As the cooler local blackbody peak of the disequilibrium model more closely overlaps with the opaque window in the disequilibrium model between 4.5-5 μm , its atmosphere is still convective in these pressures, while the equilibrium model is radiative. At pressures lower than ~ 0.8 bars, both atmospheres are radiative as more transparent windows start appearing in longer wavelengths with decreasing pressure. With these differences in the $T(P)$ profile and convective/radiative zones between models with chemical equilibrium and disequilibrium, the next important question to be investigated is whether gases like CO, NH_3 , and H_2O are quenched in the radiative or convective zones of models with chemical disequilibrium. Results from our model grid on this question are presented next.

3.2. Quenching in the Radiative Zone or the Convective Zone ?

Quenching of gases can occur in convective zones or radiative zones. Vertical mixing in convective zones is expected to be very efficient, yielding a high K_{zz} and correspondingly low t_{mix} . The top three panels of Figure 4 show the $T(P)$ profile of a brown dwarf with T_{eff} of 700 K and $\log(g)$ of 4.5 (left panel), the mixing and chemical timescales (t_{mix} and t_{chem}) for the same brown dwarf (middle panel), and the volume mixing ratios of various molecules (right panel) in the brown dwarf atmosphere. This brown dwarf has a single convective and radiative zone. The mixing timescale t_{mix} is shown in dashed black whereas the t_{chem} for CO and other chemical reactions are shown with different colors of dashed lines. The t_{mix} profile has been calculated using mixing length theory in the convective zone and with Equation 3 in the radiative zone. The mixing timescales in radiative zones are expected to be longer at depth, due to the lack of efficient dynamical mixing processes. However, as briefly described in §2, the mixing timescale is expected to be short in the much lower pressure regions ($P \sim 10^{-4}$ bars) due to the presence of gravity wave breaking mechanisms

(Freytag et al. 2010; Moses et al. 2005, 2011).

t_{mix} is much longer than t_{chem} at pressures > 100 bars and therefore CO and CH_4 are expected to follow chemical equilibrium in these high pressure high temperature parts of the atmosphere. But the t_{chem} for $\text{CO} \leftrightarrow \text{CH}_4$ reaction is a very strong function of both temperature and pressure (Zahnle & Marley 2014). Therefore, it increases by 12 orders of magnitudes within one order of magnitude in pressure and a change of 500 K in temperature. As a result, the two timescales cross each other at about ~ 30 bars at the quench pressure (P_Q). The abundances of both of these molecules, and H_2O , are quenched to constant values above P_Q as a result, as shown in the Figure 4 top right panel. As different net chemical reactions proceed at different rates and have *different* t_{chem} , their P_Q will also be different.

Self-consistent chemical equilibrium models of T-dwarfs with T_{eff} within the range of 400–800 K have shown the presence of an upper detached convective zone in addition to the deeper convective zone (Burrows et al. 1997; Marley et al. 2021), with a radiative zone in between. The $T(P)$ profile in this scenario is shown in Figure 4 bottom left panel for a brown dwarf with T_{eff} of 700 K (as above) but with a $\log(g)$ of 5.25. This detached zone appears when the $T(P)$ profile of the atmosphere is such that the radiative energy transport in the deeper atmosphere becomes efficient due to the opening of a molecular opacity window at near infrared wavelengths (Marley & Robinson 2015), as shown in Figure 4. The resulting “sandwiched radiative zone” is very likely to have a much slower rate of vertical mixing (longer t_{mix}) compared to the convective zones. As these radiative zones appear at high pressures ($P \geq 10$ bars), it is possible that molecules like CO, CH_4 and NH_3 are quenched in the radiative zone instead of the convective zone. Note that the mixing timescale profile in the upper middle panel in Figure 4 shows a “kink” like structure in t_{mix} values between 10-30 bars. This kink is due to the decrease in the convective heat flux (F in Equation 2) in the convective zone around that region. This can happen in convective regions where a non-negligible, but smaller than the convective heat transport, amount of energy transfer in a convective zone still occurs via radiation. This leads to a smaller convective heat flux in these regions.

The bottom middle panel of Figure 4 shows this scenario. Within our modeling framework, the t_{mix} is low (high K_{zz}) in the deep convective zone and t_{mix} is high (low K_{zz}) in the deep sandwiched radiative zone. The P_Q for CO in this case is within the sandwiched radiative zone. Therefore, if one is trying to probe the K_{zz} of this hypothetical object with constant K_{zz} models (e.g. Miles et al. 2020), one would infer a much lower K_{zz} than what is expected from Equation 2. However, the reason for this is not because of sluggish mixing in the convective zone but rather quenching is occurring in a radiative zone where mixing is expected to be sluggish.

Such a scenario was suggested in fits to observations presented in Miles et al. (2020). They inferred the K_{zz} for several late T and early Y-dwarfs and found that the K_{zz} for objects with T_{eff} between 400-800 K are much smaller than expectations from mixing length theory. Although equilibrium chemistry models find the sandwiched radiative zone between T_{eff} of 400–800 K (e.g. Marley et al. 2021; Allard et al. 2012), it is not clear if

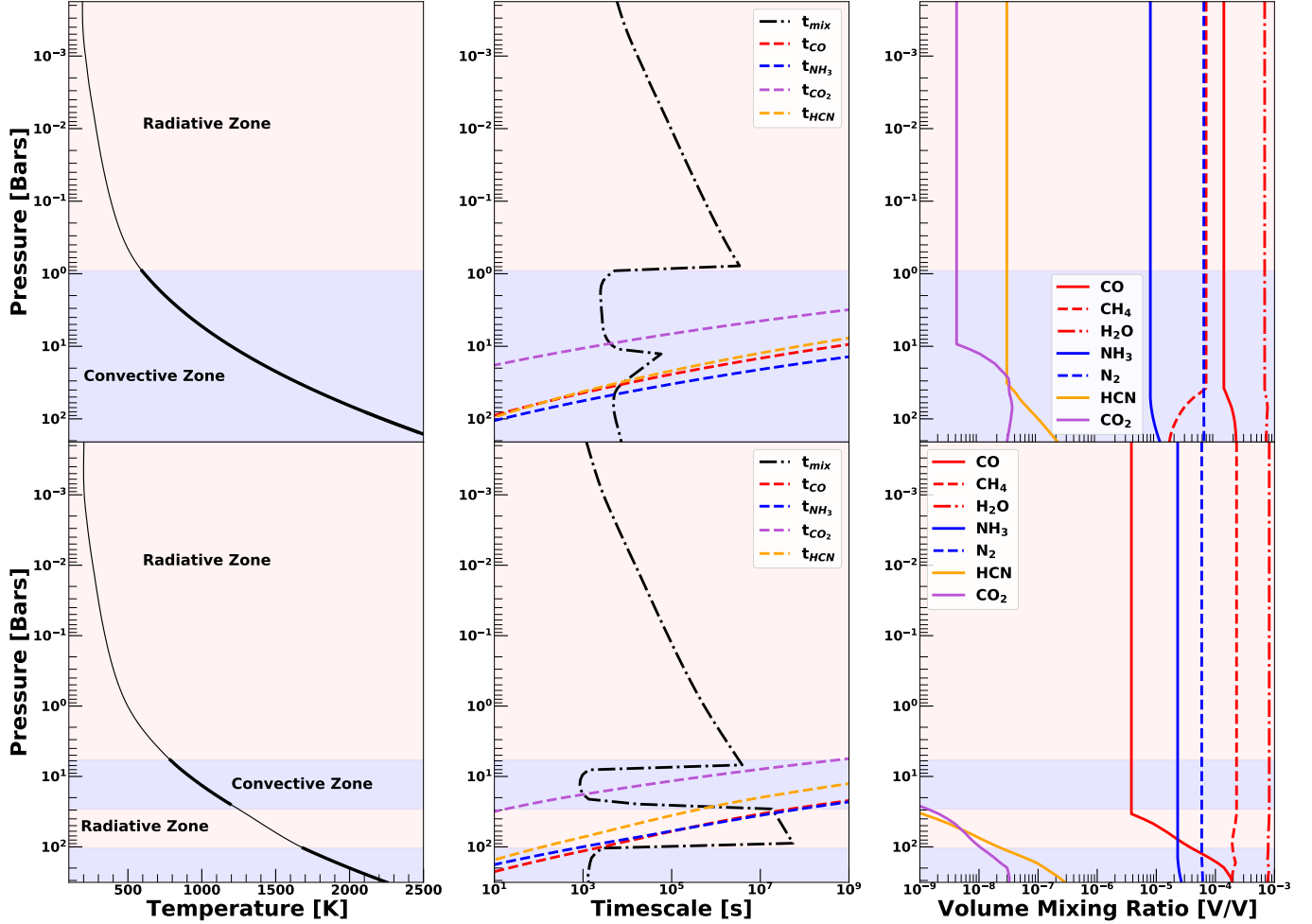


Figure 4. Model $T(P)$ profile, chemical and dynamical timescales, and chemistry for a brown dwarf with $T_{\text{eff}} 700$ K and $\log(g) = 4.5$ is shown in the top panels whereas the same properties for a brown dwarf with $T_{\text{eff}} 700$ K and $\log(g) = 5.25$ is shown in the bottom panels. $T(P)$ profile of the two brown dwarfs are shown in the **left panels** – one with a single deep convective zone while another with a deep “sandwiched” radiative zone between two deep convective zones. The **middle panels** show the comparison between the mixing timescale (black) and the chemical timescales of different gases like CO and NH_3 as a function of pressure for each of the $T(P)$ profiles shown in the left columns. The **right panels** show the volume mixing ratios of various molecules as a function of pressure for each atmosphere. **Main Point** – Gases can be quenched in a deeper “sandwiched” radiative zone in some brown dwarfs, where mixing timescales can be orders of magnitude larger than in convective zones.

the self-consistent treatment of disequilibrium chemistry preserves these sandwiched radiative zones and also if molecules like CO or NH_3 actually quench in these sandwiched radiative zones. Next, we investigate this scenario in more detail.

We can expand the modeling work shown in Figure 4 over a range in T_{eff} and $\log(g)$ to assess under what conditions a sandwiched radiative zone occurs in self-consistent non-equilibrium models. Figure 5 shows the appearance of the sandwiched radiative zones across this phase space in the presence and absence of vertical mixing. The colors shown in Figure 5 represents $\log_{10}(P_{\text{bot}}/P_{\text{top}})$ where P_{bot} and P_{top} are the pressures at the bottom and top of the sandwiched radiative zone, respectively. If the model does not find a sandwiched radiative zone, this number will be zero. The top panel in Figure 5 shows the sandwiched radiative zones in chemical equilibrium models. The other three panels show the appearance of the second radiative zone with three different magnitudes of mixing in the radiative zone, all assuming the mixing length L is H in the convective region.

Under the assumption of equilibrium chemistry it is clear that the sandwiched radiative zones appear between T_{eff} of 450-800 K for a $\log(g)$ of 4.5. However, for objects with $\log(g)$ of 4.75 and higher, the sandwiched radiative zones only appear between 450-600 K in chemical equilibrium models. For models with disequilibrium chemistry, the models that show the presence of this sandwiched radiative zone appear at a different set of T_{eff} and $\log(g)$ values. As can be seen in Figure 5 (second, third, and fourth panels), high gravity models with $\log(g)$ of 5.0 and greater have this sandwiched radiative zone between T_{eff} of ~ 500 -800 K. For models with $\log(g)$ of 4.75 the sandwiched radiative zone appears between 500-750 K. However, for models with $\log(g)$ of 4.5, the sandwiched radiative zone is non-existent when quenching due to vertical mixing is taken into account. The thickness of these zones is typically smaller, too, as can be seen from the shading that is less yellow.

Figure 6 shows the appearance of this sandwiched radiative zone if the convective mixing length L is smaller, only $0.1 \times H$. The second, third, and fourth panels in

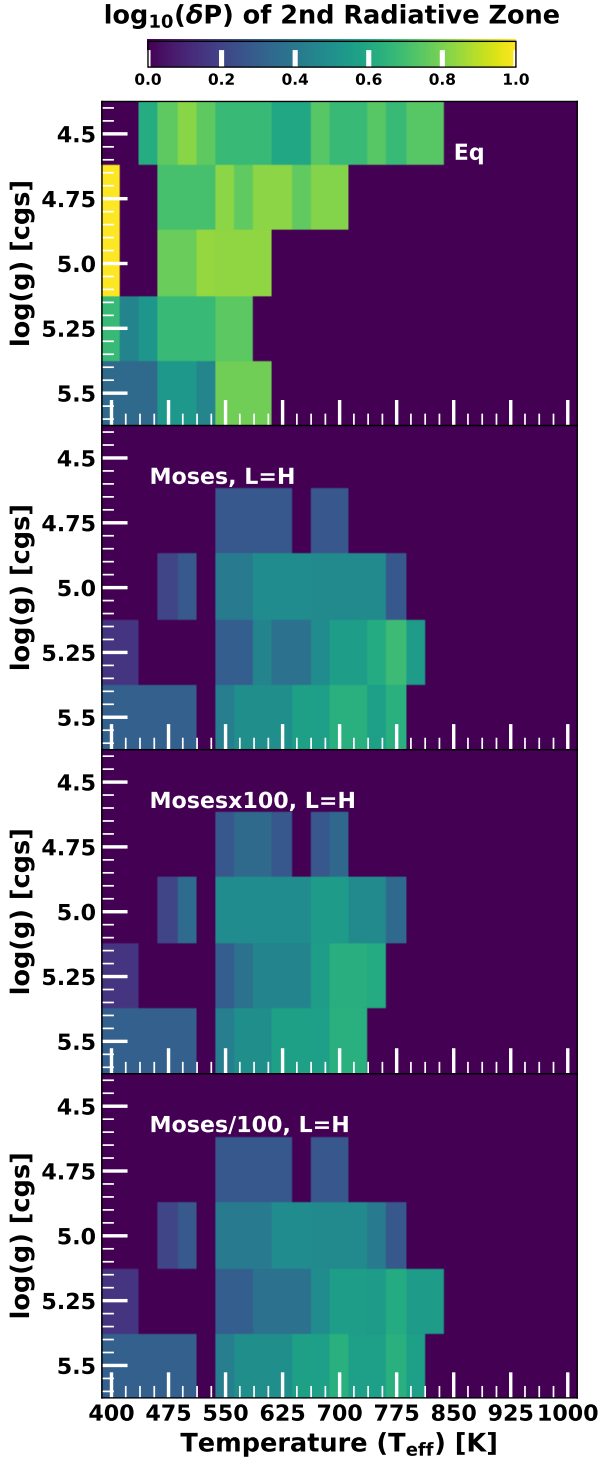


Figure 5. Appearance of the 2nd radiative zone in the T_{eff} vs. $\log(g)$ parameter space in our grid is shown. The colors show the value of the quantity $\log_{10}(P_{\text{bot}}/P_{\text{top}})$ where P_{bot} and P_{top} are the pressures at the bottom and top of the sandwiched radiative zone, respectively. The **top panel** shows this in case of equilibrium chemistry. The subsequent panels show the presence of the 2nd radiative zone if different vigor of K_{zz} is chosen keeping the convective zone mixing length fixed at H . Dark blue indicates no second convective zone at depth.

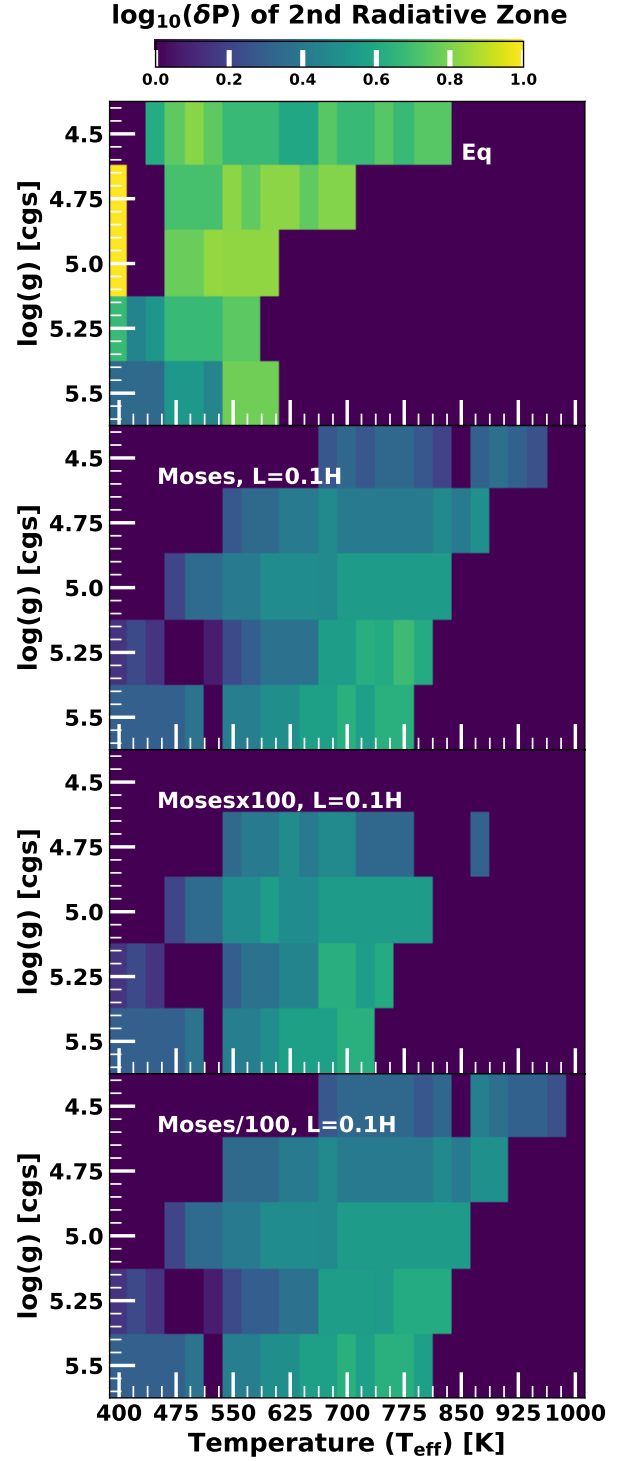


Figure 6. Appearance of the 2nd radiative zone in the T_{eff} vs. $\log(g)$ parameter space in our grid is shown. The colors show the value of the quantity $\log_{10}(P_{\text{bot}}/P_{\text{top}})$ where P_{bot} and P_{top} are the pressures at the bottom and top of the sandwiched radiative zone, respectively. The **top panel** shows this in case of equilibrium chemistry. The subsequent panels show the presence of the 2nd radiative zone if different vigor of K_{zz} is chosen keeping the convective zone mixing length fixed at $0.1 \times H$. Dark blue indicates no second convective zone at depth.

Figure 6 show that larger number of models now develop this sandwiched radiative zone compared to models with $L = H$ shown in Figure 5. The sandwiched radiative zone does indeed appear at low gravity ($\log(g) = 4.5$) when $L = 0.1 \times H$. Additionally, the radiative zones tend to appear at higher T_{eff} than for $L = H$ models. This shows that the strength of vertical mixing in both the radiative and convective zone can influence the presence and absence of multiple convective zones.

The effect of radiative and convective K_{zz} on the chemical abundances is more complex than it may appear. The presence of a sandwiched radiative zone does not guarantee that quenching occurs in the radiative zone. Furthermore, radiative zone quenching can also occur in atmospheres with a single radiative zone and single convective zones. We investigate the resulting photospheric CO abundances in T_{eff} vs. $\log(g)$ space in Figure 7. The top panel shows the CO abundance in models in chemical equilibrium. The second, third, and fourth panels show models with disequilibrium chemistry. Each of these panels represents models with different values of K_{zz} in the radiative zone while the mixing length in the convective zone is fixed to H . Models where CO, CH_4 , and H_2O are quenched in radiative zones are marked with black hatches. The rest of the models still have CO quenching, but in the convective zones instead.

The CO abundances in these models with radiative zone CO quenching also show large differences from CO abundances in models with convective zone quenching. These differences appear as discontinuities in the CO abundance heat map shown in the second, third, and fourth panels of Figure 7. The reason behind these discontinuities is mainly the smaller P_Q of CO in models with radiative zone quenching compared to models with convective zone quenching.

However, Figure 8 shows that CO abundances over T_{eff} and $\log(g)$ will change if the mixing length in the convective zone is smaller. Here, again, $L = 0.1 \times H$, leading to smaller K_{zz} values, and longer t_{mix} in the convective zone. This causes quenching to often occur in the top or sandwiched radiative zone in a significantly larger fraction of the T_{eff} and $\log(g)$ parameter space compared to the nominal $L = H$ scenario in Figure 7. For models with $\log(g)=4.75$ and greater, all models with $T_{\text{eff}} \geq 550$ K show radiative zone quenching of CO and CH_4 in this case. Both Figure 7 and 8 makes it clear that the chemical properties of brown dwarfs that will have either radiative zone or convective zone quenching depends on the vigor of mixing in both of these types of zones.

Furthermore, since t_{chem} , and hence the P_Q , of different gaseous species are different, this means that models where CO quenches in radiative zones are not necessarily models where CO_2 or NH_3 also quenches in the radiative zone. This effect can be clearly seen in Figure 9, which shows the same set of models in Figure 7, but now with the CO_2 abundances and its radiative/convective quench behavior. Because the t_{chem} for the thermochemical equilibrium of CO_2 is orders of magnitude shorter than for CO and CH_4 , the models where CO_2 quenches in the radiative zone are also different than those where CO/ CH_4 quenches in the radiative zone. If the mixing length in the convective zone is H , CO_2 radiative zone quenching occurs mostly in models that are hotter than 700 K and have gravity higher than $\log(g)$ of 5. The same

effect for quenching of NH_3 has been shown in Figure 10 in models with $L = 0.1 \times H$. Comparing Figure 10 with 8 shows that the radiative zone quenching of NH_3 occurs in only a small subset of lower temperature (500–800 K) models with radiative zone quenching of CO, when $L = 0.1 \times H$. The t_{chem} for the reaction between $\text{N}_2 \leftrightarrow \text{NH}_3$ is the slowest among the other reactions described in §2.1. As a result, if $L = H$, NH_3 always gets quenched in the deep convective zone in the parameter space explored by our grid. Even if the convective mixing length is smaller ($L = 0.1 \times H$), NH_3 gets quenched in the convective zone of the majority of the models except in some where deeper “sandwiched” radiative zones develop. But in order to measure these quenched abundances observationally and infer the K_{zz} profile of the atmosphere, we need to investigate the effect of K_{zz} on observables, such as the emission spectra of these brown dwarfs, which we discuss next.

3.3. Effect of Radiative and Convective Zone K_{zz} on Emission Spectra

We have established in §3.2 that gases like CO, CH_4 and CO_2 can be quenched in the sandwiched radiative zones or single radiative zones in a subset of late T and early L-dwarfs. In Figures 11, 12, and 13, we show how thermal emission spectra are sensitive to the vigor of vertical mixing in the radiative zone of these objects. These spectra, with a spectral resolution of 600, are calculated using the thermal emission calculation module of PICASO (Batalha et al. 2019), using the same opacities that were used for model convergences to RCE. Sources of these opacities can be found in Marley et al. (2021).

The thermal emission spectra between 4.2-5.0 μm , across a range of T_{eff} between 400 K and 1000 K with steps of 100 K, are shown for $\log(g)$ values of 5 and 5.5 in the two upper panels of Figure 11. The choice of the wavelength range focuses on the role of CO, which has significant impacts on the spectrum in M-band between 4.4-5 μm . H_2O is the primary absorber between 4.0-4.4 μm . These models assume $L = H$ in the convective zones. Figure 11 lower panels shows the spectrum from the same set of models except $L = 0.1 \times H$. Spectra arising from different vigors of vertical mixing in the radiative zones are shown with different line dashes in all the panels.

Sensitivity of the M-band spectrum to radiative zone K_{zz} values is more common for higher gravity objects with $\log(g)$ of 5.0 and 5.5. If the convective mixing length is H , then this sensitivity appears between models with T_{eff} 550- 700 K for $\log(g)$ of 5. However, if the convective mixing length is $0.1 \times H$, then this sensitivity appears much more commonly between models with T_{eff} of 500-1000 K for $\log(g)= 5.0$. At higher gravity, $\log(g)$ of 5.5, the sensitivity of M-band spectra to radiative zone K_{zz} appears at both convective mixing lengths of H and $0.1 \times H$. In Figure 11 upper right panel, this sensitivity appears between 500-900 K whereas in Figure 11 lower right panel this sensitivity appears between 500-1000 K.

While the M-band shows the greatest sensitivity to K_{zz} in the radiative and convective zones, smaller differences in the spectra arise in other wavelengths as well. Figure 12 top panels shows the sensitivity of the H-band spectra to the radiative zone K_{zz} across various values of T_{eff} for brown dwarf models with $\log(g)=5.0$. The top left panel

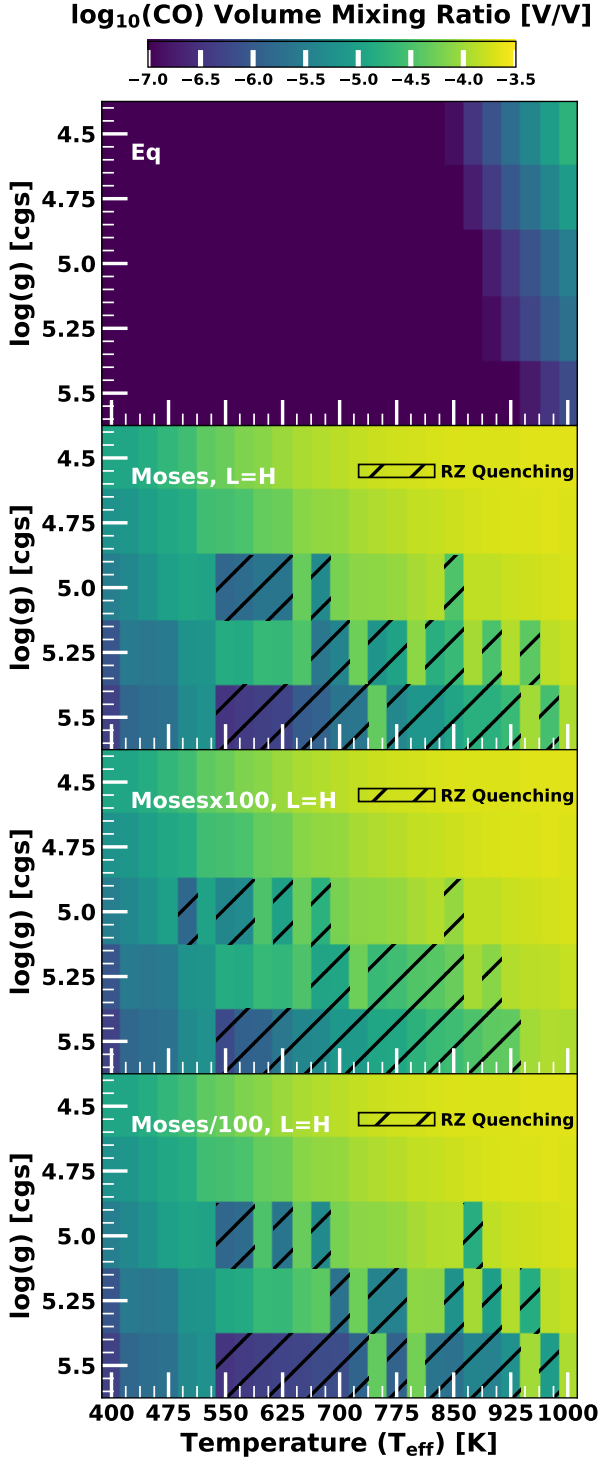


Figure 7. Top panel shows the equilibrium chemistry abundance of CO at pressures where $T = T_{\text{eff}}$ in our T_{eff} vs. gravity grid of chemical equilibrium models. The second, third and last panels depict the quenched CO abundance within the T_{eff} vs. gravity parameter space in our disequilibrium chemistry models. The second, third and last panels correspond models with radiative zone K_{zz} values of “Moses”, “Moses \times 100”, and “Moses/100”, respectively while the convective zone mixing length L was fixed at the scale height H . Models where CO was quenched at the radiative zone are marked with black hatches. CO was quenched at a convective zone in the rest of the models. Models with radiative zone CO quenching show much smaller CO abundance compared to models with convective zone quenching.

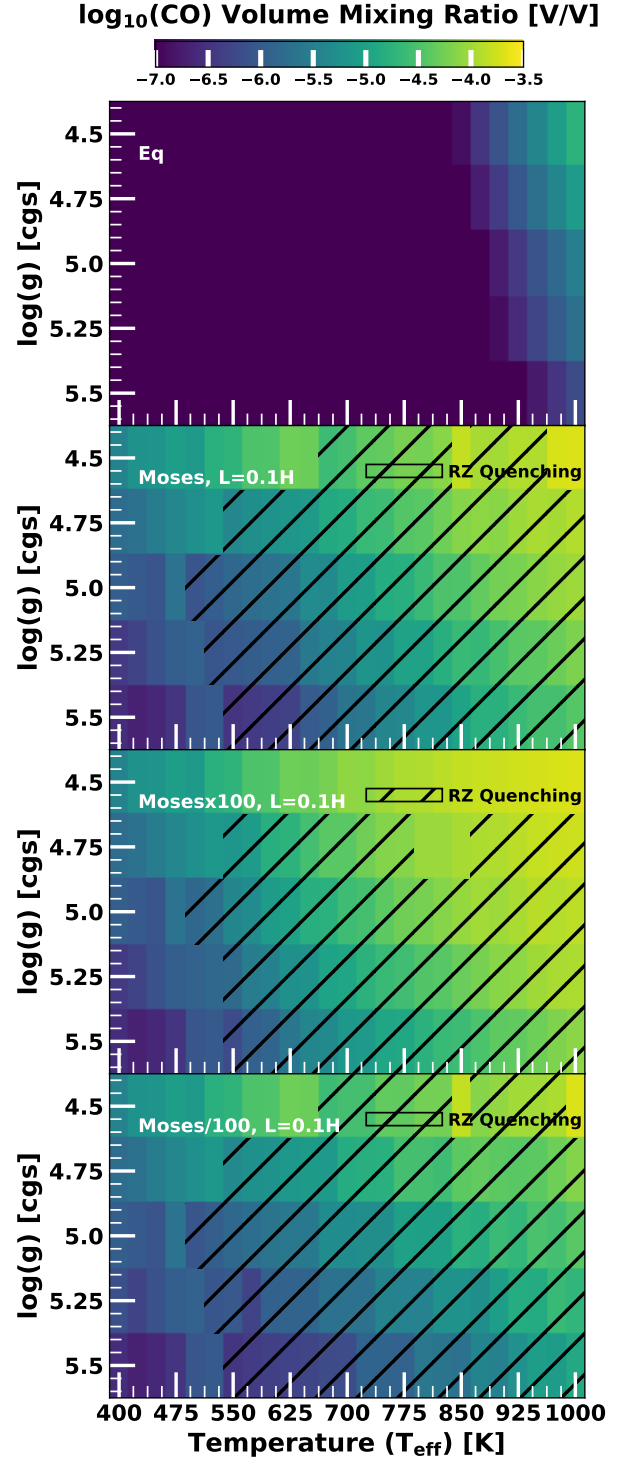


Figure 8. Same as Figure 7 except with the mixing length in convective zones fixed at $0.1 \times H$. In these models CO is mostly quenched in a radiative zone.

shows models with $L = H$ whereas the top right panel shows models with $L = 0.1 \times H$. The sensitivity mainly appears between $1.69 \mu\text{m}$ and $1.75 \mu\text{m}$ in models where CH_4 is quenched in the radiative zone as it is the main opacity source at these wavelengths. CH_4 is also the main opacity source between $2\text{--}2.2 \mu\text{m}$, $3.2\text{--}3.5 \mu\text{m}$, and $3.5\text{--}4 \mu\text{m}$. As a result, the spectra at these wavelength

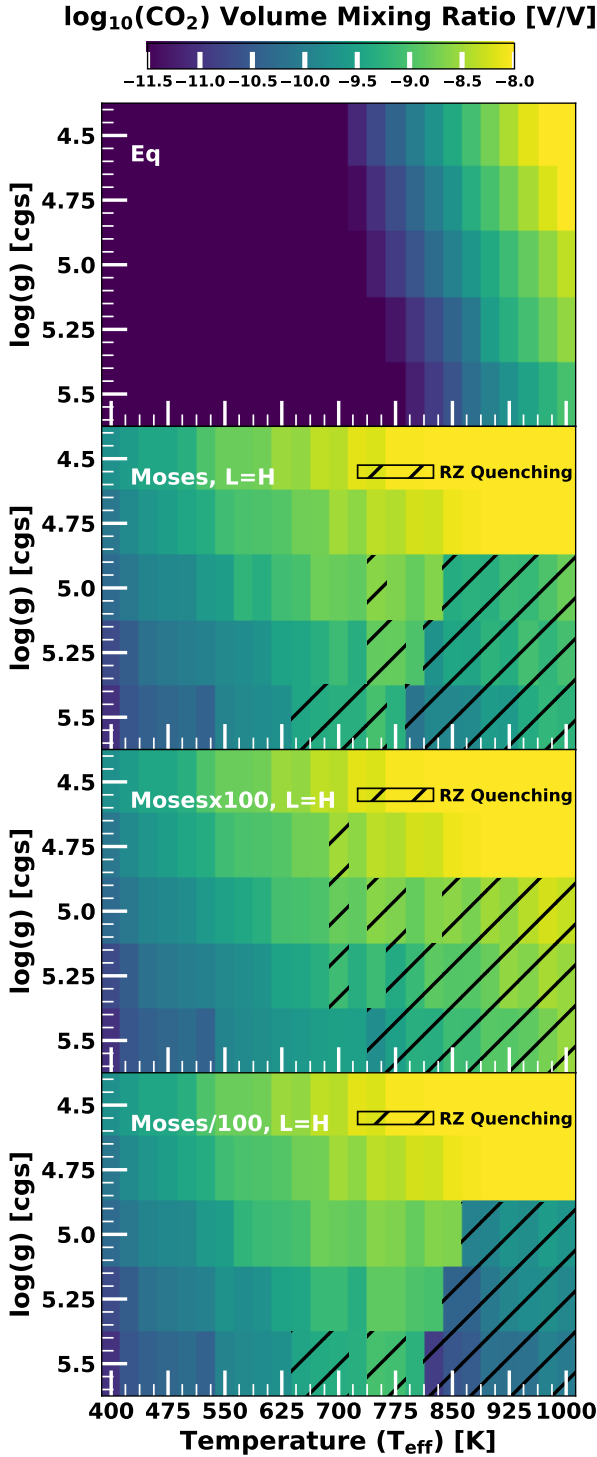


Figure 9. Same as Figure 7 but for quenching of CO_2 . Given the different t_{chem} for CO_2 , compared to CO , the quench levels are entirely different.

ranges also show some sensitivity to the radiative zone K_{zz} of the deep atmosphere. This sensitivity between $2\text{--}2.2\ \mu\text{m}$, $3.2\text{--}3.5\ \mu\text{m}$, and $3.5\text{--}4\ \mu\text{m}$ is shown in Figure 12 bottom panels and Figure 13 top and bottom panels, respectively. Examining different spectral regions for a given object, that are sensitive to both CH_4 and CO , will help in constraining the radiative zone K_{zz} , as both

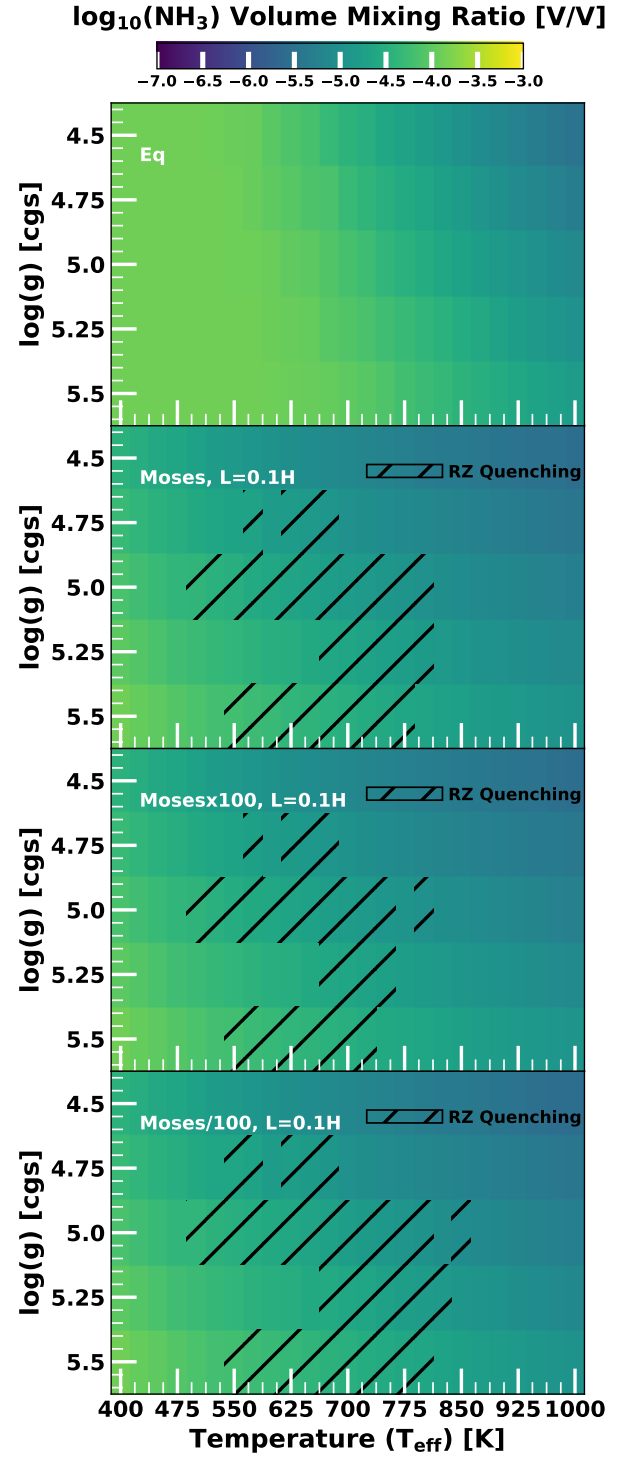


Figure 10. Same as Figure 8 but for quenching of NH_3 . Given the different t_{chem} for NH_3 , compared to CO , the quench levels are entirely different.

gas species abundances can be used as probes. Apart from the emission spectra itself, other observables like broadband IR colors and magnitudes of brown dwarfs are also known to be sensitive to K_{zz} (e.g. Saumon et al. 2003; Karalidi et al. 2021), which we explore next.

3.4. Color Magnitude Diagrams

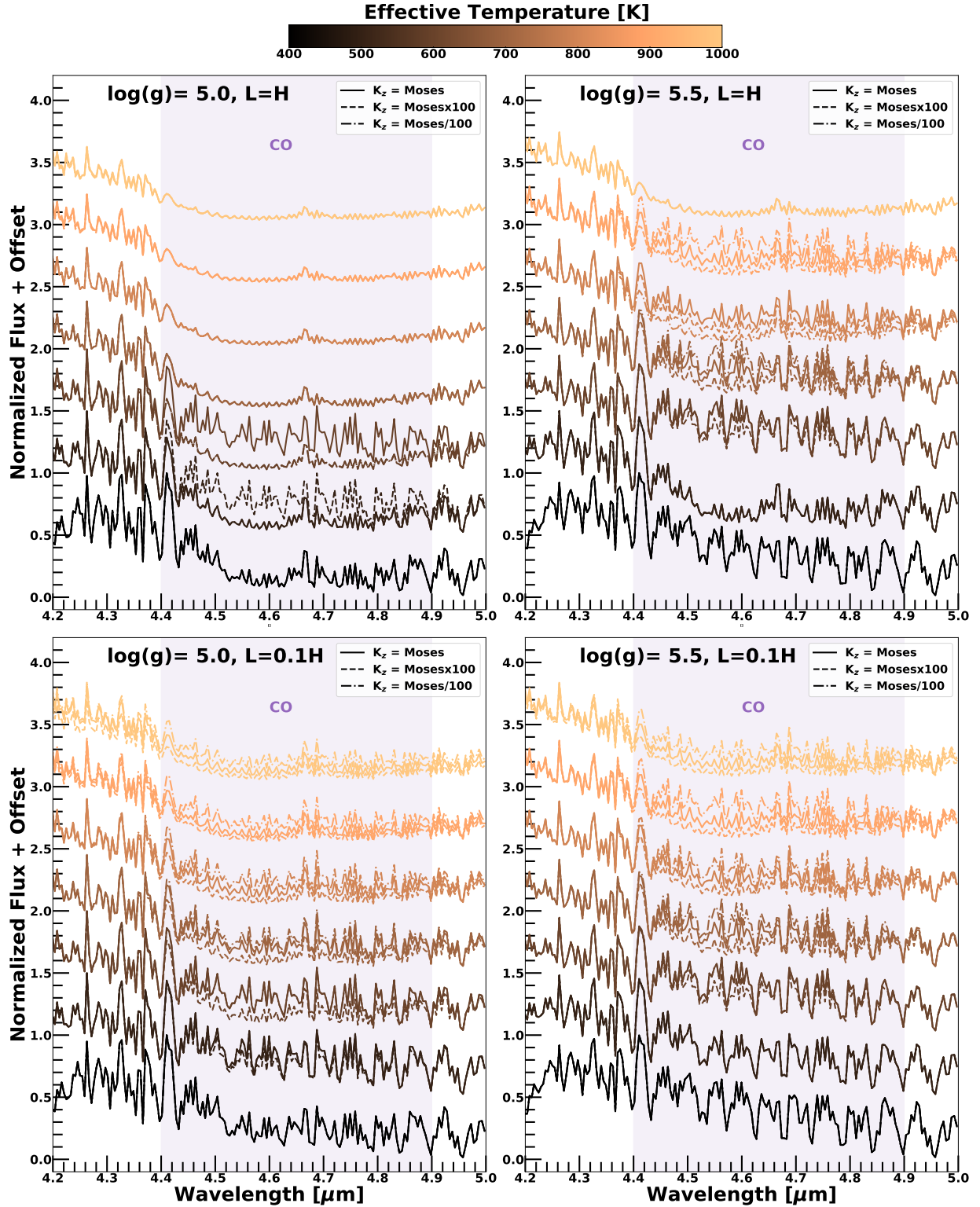


Figure 11. M-band Thermal emission spectra across a range of T_{eff} between 400 K and 1000 K with steps of 100 K are shown in each panel. $\log(g) = 5.0$ is on the left and 5.5 is on the right. The colors are representative of the T_{eff} . The models shown in the upper left and right panels assume the convective mixing length L to be H whereas the models shown in the lower left and right panels assume $L = 0.1 \times H$. The three line styles show different radiative zone K_{zz} parametrizations, including Moses (solid), Moses/100 (dashed), and Moses \times 100 (dash-dot). If quenching occurs in a convective zone the three spectra plot atop each other. The shaded region shows the wavelength range where CO is the most important absorber.

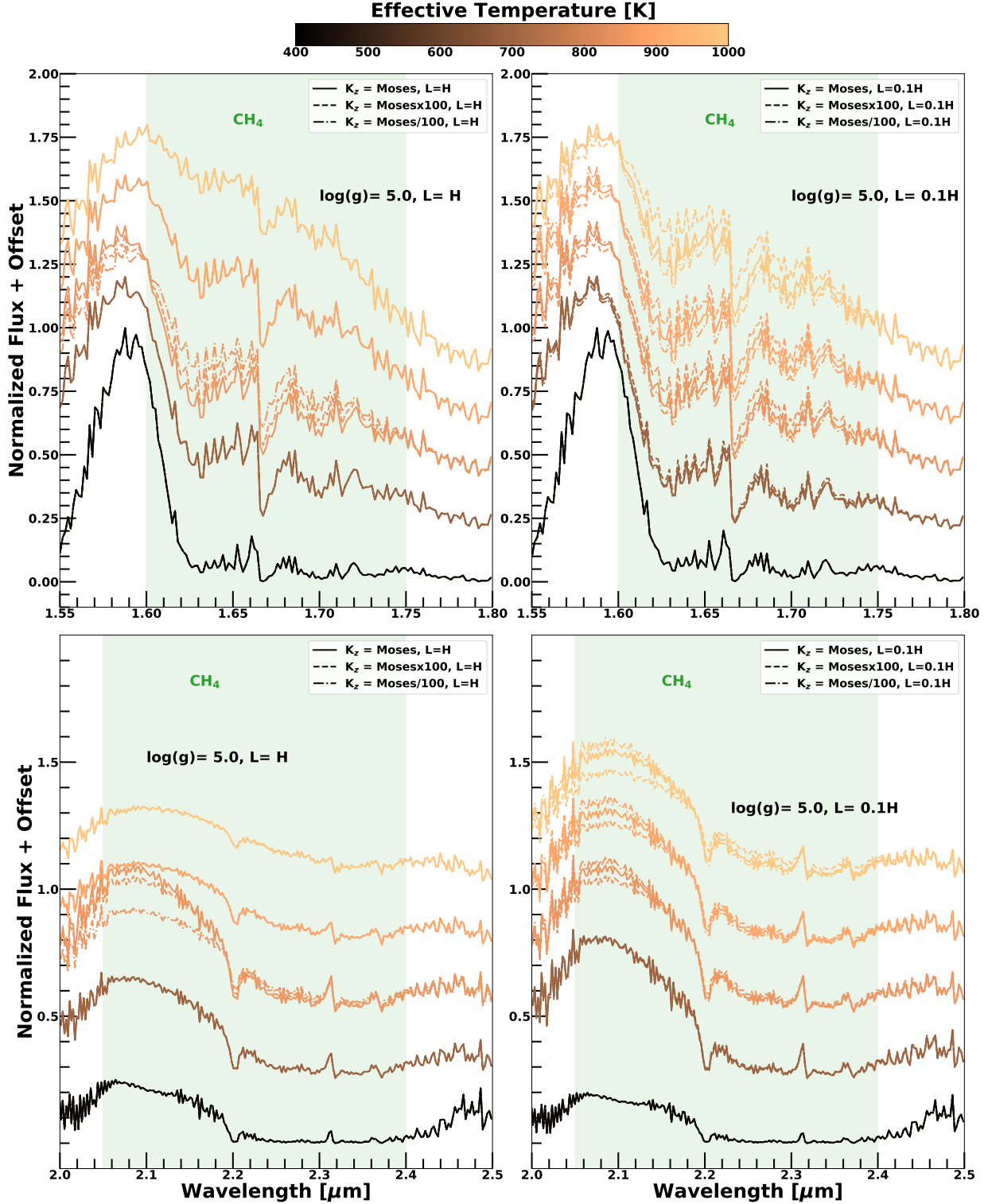


Figure 12. H-band thermal emission spectra of models from our grid are shown in the top left and right panels whereas the bottom left and right panels show the K-band emission spectra. Models with $\log(g)=5$ and different T_{eff} between 400-1000 K are shown in each panel. From bottom to top, spectra for T_{eff} values of 425 K, 700 K, 850 K, 900 K, and 1000 K are shown in all the panels. **Top left panel** shows the thermal emission spectra of models which have convective mixing length set at H but have different K_{zz} parametrizations like Moses, Moses/100, and Moses \times 100 which are represented by different line types in the panels like solid, dashed, and dashed-dotted. **Top right panel** shows the same but for models with convective mixing length set at $0.1 \times H$. **Bottom left and right panels** show the sensitivity of the K band spectrum to radiative zone K_{zz} when $L = H$ and $L = 0.1 \times H$, respectively. The shaded region shows the wavelength range where CH₄ is the most important absorber.

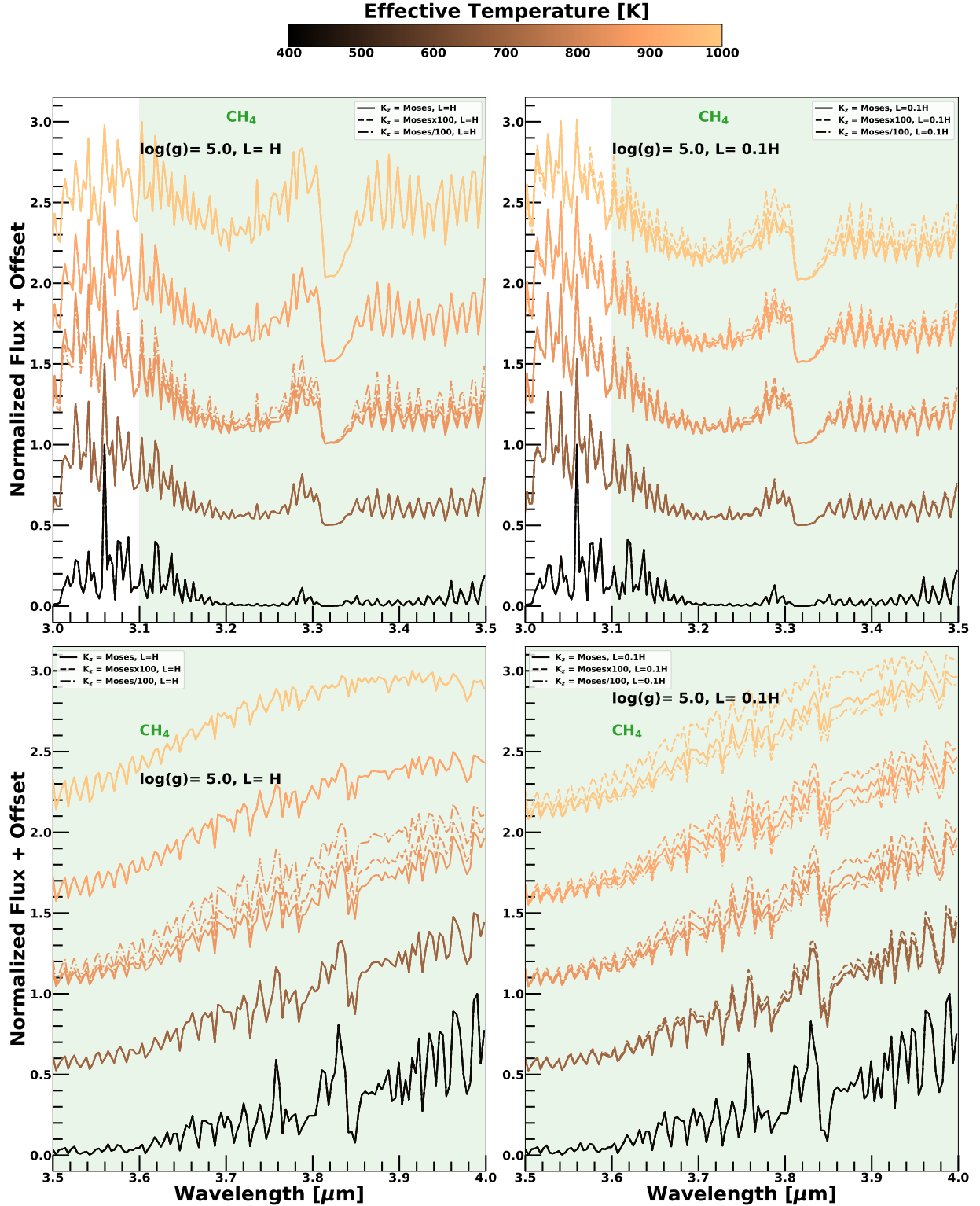


Figure 13. Thermal emission spectra of brown dwarfs between 3 and 3.5 μm are shown in the top left and right panels. Emission spectra of the same models in the L-band are shown in the bottom left and right panels. Models with $\log(g)=5$ and different T_{eff} between 400-1000 K are shown in each panel. From bottom to top, spectra for T_{eff} values of 425 K, 700 K, 850 K, 900 K, and 1000 K are shown in all the panels. **Top left panel** shows the emission spectra of models which have convective mixing length set at H but have different K_{zz} parametrizations like Moses, Moses/100, and Moses \times 100 which are represented by different line types in the panels like solid, dashed, and dashed-dotted. **Top right panel** shows the same but for models with convective mixing length set at $0.1 \times H$. **Bottom left and right panels** show the sensitivity of the L-band spectrum to radiative zone K_{zz} when $L = H$ and $L = 0.1 \times H$, respectively. The shaded region shows the wavelength range where CH_4 is the most important absorber.

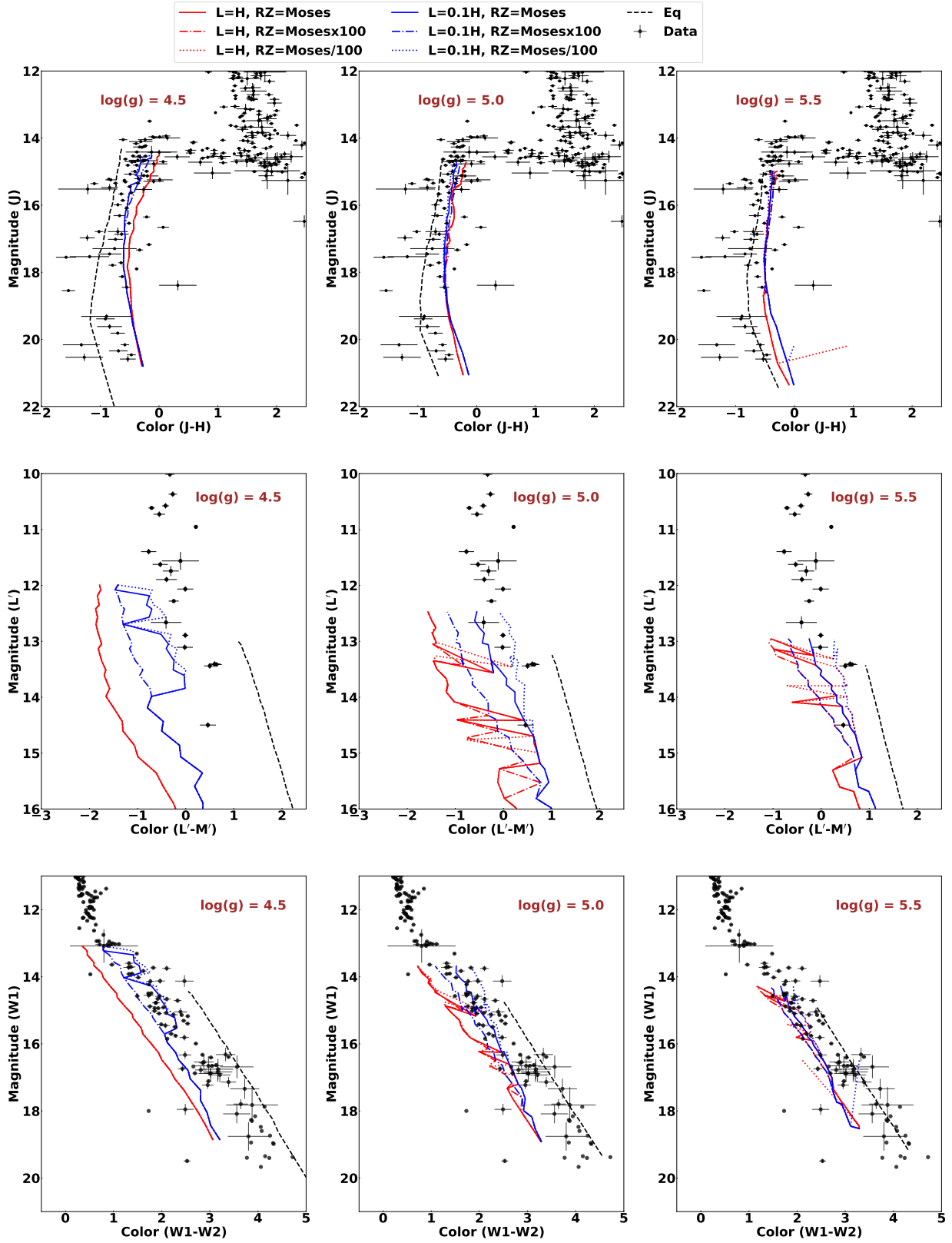


Figure 14. Color magnitude diagrams (CMD) of observed brown dwarfs in different filters are shown with overplotted equilibrium and disequilibrium chemistry model tracks with different strengths of convective and radiative zone vertical mixing. The top row shows the J vs. J-H where the models with convective zone mixing length of H and different radiative zone K_{zz} are shown with various linetypes of red. Models with convective zone mixing length of $0.1 \times H$ and different radiative zone K_{zz} are shown with various linetypes of blue and the equilibrium chemistry models are shown with dashed black lines. Each column shows the same data but the model tracks with different values of $\log(g)$. The second row shows the the L' vs $L'-M'$ whereas the third row shows the W1 vs. W1-W2.

Coupling our atmospheric model grid with brown dwarf evolutionary models from Marley et al. (2021) enables us to generate color magnitude diagrams (CMDs) of these brown dwarfs. These evolutionary models track the T_{eff} , $\log(g)$ and bolometric luminosity as a function of age for each brown dwarf mass. The procedure is the same as in Marley et al. (2021), although our models here are slightly not self-consistent, as the upper boundary condition for the Marley et al. (2021) cooling tracks assume equilibrium chemical abundances.

Figure 14 shows the observed CMD of brown dwarfs in various standard infrared filter combinations. We show J vs. J-H, MKO L' vs. L'-M', and WISE W1 vs. W1-W2 in the first, second and third rows, respectively. The mid-infrared wavelengths are most sensitive to disequilibrium chemistry effects. Model tracks for three different $\log(g)$ (4.5, 5.0 and 5.5) values are shown in the three columns for each combination of filters. The database maintained by Trent Dupuy¹ (Dupuy & Liu 2012; Dupuy & Kraus 2013; Liu et al. 2016) has been used for the observational data. The red model tracks in all the panels represents models with convective mixing length set at H whereas the blue tracks represents models with convective mixing length set at $0.1 \times H$. Each line type (solid, dotted, and dash-dotted) in both of these colors represents models with the different radiative zone K_{zz} values “Moses $\times 100$ ”, “Moses”, and “Moses/100,” respectively. The black dashed lines represents CMD tracks from equilibrium chemistry models.

In the J vs. J-H filter combination CMD, it appears that models treating disequilibrium chemistry self-consistently provide a slightly better fit to the observed photometry than the equilibrium chemistry, for models at $\log(g)$ of 5.0-5.5, representative of the field sample. The disequilibrium chemistry models with different convective mixing lengths shown by the blue and red tracks almost fall on top of each other as the J and H band fluxes are not particularly sensitive to CO abundance but has some sensitivity to CH_4 abundance.

The chemical equilibrium model CMD tracks follow a much redder sequence in the MKO L' vs. L'-M' CMDs compared to the observed photometry. The disequilibrium chemistry models are comparatively much bluer. As discussed in the previous sections, enhanced CO abundance in disequilibrium chemistry model causes the M'-band and the W2-band fluxes to be fainter than equilibrium chemistry models. On the other hand, depleted CH_4 abundance in disequilibrium chemistry models causes higher fluxes in the L' and W1 bands. Both of these effects causes the disequilibrium model tracks (shown with red and blue lines) to be significantly bluer than the equilibrium chemistry model tracks (shown with black line) in the L' vs. L'-M' and W1 vs. W1-W2 CMD.

It is interesting to note the non-monotonic behavior. At higher gravity ($\log(g) = 5.0$ and 5.5) some disequilibrium chemistry models show radiative zone quenching instead of convective zone quenching. As a result, these atmospheres have lower photospheric CO compared to disequilibrium chemistry with convective quenching, but a much higher CO abundance compared to the equilibrium chemistry models. Therefore, the models with ra-

diative zone quenching are redder than disequilibrium chemistry models with convective zone quenching but bluer than equilibrium chemistry models, “jutting out” to the red for some models.

The second and third rows in Figure 14 also show that disequilibrium models with $L = H$ with convective zone quenching of CO are much bluer than the observed sequence. However, disequilibrium models with $L = 0.1 \times H$ provide a generally better fit to the mid-IR photometry. This suggests that longer t_{mix} values in the deeper atmosphere provide a better fit to the photometry from the T and Y dwarf population, than the t_{mix} calculated from assumptions like free convection. However, this result is empirical in nature and needs further validation from 3D tracer transport models like in Bordwell et al. (2018). Coupling our models with 1D chemical kinetics models will also help us in interpreting these trends better, which is something we will address in future studies. It seems clear that even lower K_{zz} values for the faintest models may be necessary, as the data are generally more consistent with equilibrium chemistry models at $\log(g)$ of 5.0-5.5. We also note that we have not included clouds within our models and they might have some impact on the model magnitudes presented here especially for the faintest end of these tracks as H_2O clouds are expected to form in the colder objects ($T_{\text{eff}} \leq 450$ K) (Morley et al. 2014).

3.5. Comparing to Spectroscopic Observations

We use our grid of atmosphere models to compare with ground-based spectral observations of six late T and early Y-dwarfs. We aim to determine the atmospheric properties of brown dwarfs – Gleise 570 D (Burgasser et al. 2000), 2MASS J0415-0935 (Burgasser et al. 2002), WISE 0313 (Kirkpatrick et al. 2011), UGPS 0722 (Cushing et al. 2011), WISE 2056 (Schneider et al. 2015), and WISE 1541 (Schneider et al. 2015) with our models. Although Miles et al. (2020) had the Y-dwarf WISE 0855 in their sample, we exclude this object from our analysis as it is expected to have optically thick water clouds in its atmosphere due to its cold T_{eff} (~ 250 K) and our model grid only extends to a $T_{\text{eff}} = 400$ K. As noted in §3, this choice for the lower bound on T_{eff} in our model grid was made because our models lack a self-consistent treatment of clouds with disequilibrium chemistry, currently.

For comparing our models with observational data, which includes both near-infrared and M-band spectra, we use the goodness of fit parameter – G_k defined as (Cushing et al. 2008),

$$G_k = \frac{1}{n - m} \sum_{i=1}^n w_i \left(\frac{f_i - C_k F_i^k}{\sigma_i} \right)^2 \quad (4)$$

where n is the number of observational data points, m is the number of free parameters being fit, w_i are the weights of fitting i 'th data point, f_i is the i 'th observed flux, F_i^k is the i 'th model flux point of the k 'th model, and σ_i is the error in the i 'th observed flux. The factor C_k is a renormalization factor for the model fluxes. If the observed fluxes are flux calibrated then C_k represents the factor R^2/D^2 but if the observed fluxes are not flux calibrated then C_k represents the factor $\alpha R^2/D^2$ where $1/\alpha$ represents the unknown flux normalization of the

¹ <http://www.as.utexas.edu/~tdupuy/plx>

observed flux. The C_k factor is given by (Cushing et al. 2008),

$$C_k = \frac{\sum_{i=1}^n w_i f_i F_i^k / \sigma_i^2}{\sum_{i=1}^n w_i (F_i^k)^2 / \sigma_i^2} \quad (5)$$

Since there is no reported bias in any of the datasets we use, w_i is always fixed at 1 for our analysis.

3.5.1. Gliese 570 D and 2MASS J0415-0935

Gliese 570 D is a T7.5 dwarf (Burgasser et al. 2006) which has a measured spectrum in the M-band with two different instruments – AKARI (Sorahana & Yamamura 2012) and GEMINI/NIRI (Geballe et al. 2009). We used the M-band spectra of Gliese 570 D reported in (Geballe et al. 2009) because it has a higher SNR ratio. We also use the NIRC 1-2.5 μm spectra of Gliese 570 D (Gl 570D) reported in Burgasser et al. (2002) and *Spitzer* Infrared Spectrograph (IRS) 5-14 μm spectra of Gliese 570 D reported in Suárez & Metchev (2022). We adopt the methodology described in Sorahana & Yamamura (2012) for fitting the spectrum of Gl 570D with our grid of models. Firstly, we use our grid of models to calculate C_k using only the M-band GEMINI/NIRI data for Gl 570D. Using this set of calculated C_k , we calculate the G_k parameter using our models and the M-band GEMINI/NIRI data for Gl 570D. Then we select all the models with values of the G_k parameter between $\min(G_k)$ and $\min(G_k) + 1$. This step gave us 131 models which best-fits the M-band GEMINI/NIRI data for Gl 570D. The G_k parameter for these 131 models are distributed between 0.9899 and 1.9550.

The top left panel of Figure 15 shows the observed M-band spectrum of Gl 570 D (Geballe et al. 2009) with red points, the observed NIRC spectrum of Gl 570 D (Burgasser et al. 2002) with black points, and the *Spitzer* IRS spectrum (Suárez & Metchev 2022) with brown points. The range of fluxes covered by the 131 best-fitting models to the M-band spectra only, are shown with the blue shaded region in the top left panel of Figure 15. All of these models fit the M-band spectrum well but differ significantly in their fluxes in the shorter and longer wavelengths. We calculate a new set of G_k parameter for these 131 models but now with the NIRC and *Spitzer* IRS data only. The set of C_k parameters for each model, determined by fitting the M-band spectra already, are re-used for this, following the methodology of Sorahana & Yamamura (2012). The model among these 131 models that fits this shorter and longer wavelength data as well (has the least G_k) is taken to be the overall best-fit model from the grid. This model spectra is shown in Figure 15 top right panel and it has a G_k value of 669.06. This large difference between the G_k values from M-band data and the NIRC+IRS data is mainly because of the large difference in the uncertainties in the fluxes from these two sets of observations.

The best-fit model has a T_{eff} of 725 K and a $\log(g)$ of 5.0. The K_{zz} in the radiative zone for this model is Moses and the convective mixing length is $0.1 \times H$. The M-band spectra of this model compared to the M-band data for Gl 570D is also shown in the bottom left panel. The $T(P)$ profile, mixing timescale and chemical timescales, as well as the mixing ratio profiles of various gases in this model are shown in the three bottom right

panels. The $T(P)$ profile and the t_{mix} profile both show that this model has two convective zones. The t_{chem} and t_{mix} shown in the middle panel of the bottom right part of Figure 15 also show that CO, CH₄, H₂O, HCN, and NH₃ are quenched in the sandwiched radiative zone for this best-fit model whereas CO₂ is quenched in the upper detached convective zone. The C_k value of this best-fit model is 1.72×10^{-19} . The measured parallax of Gl 570D is 171.22 mas (Dupuy & Liu 2012). This corresponds to a distance (D) of 5.84 pc. We get a radius of 1.04 R_J for Gl 570D combining these values together. The radius of a brown dwarf with $T_{\text{eff}}=725$ K and $\log(g)=5.0$ can also be interpolated from evolutionary grids like the SONORA BOBCAT models (Marley et al. 2021). We find this interpolated radius to be 0.89 R_J which is somewhat smaller than our calculated radius. But as we also note in §3.4, these evolutionary tracks were computed assuming chemical equilibrium.

We use the same technique for fitting the AKARI M-band spectrum (Sorahana & Yamamura 2012) and the NIRC + *Spitzer* IRS spectrum (Burgasser et al. 2002; Suárez & Metchev 2022) of 2MASS J0415-0935 (2M 0415). The top left panel of Figure 16 shows the M-band spectra of 2M 0415 with red points, the NIRC measurements are shown with black points, and the *Spitzer* IRS measurements are shown with brown points. The $\min(G_k)$ obtained by fitting the M-band spectra only is 0.8755 and the flux range covered by all the models with G_k between 0.8755 and 1.8583 is shown with the blue shaded region in the top left panel. These models were then used to obtain the best-fitting model with the low and high wavelength data. The best-fit model has a G_k of 514.28. This model has a T_{eff} of 675 K and a $\log(g)$ of 4.75. The K_{zz} in the radiative zone for this model is Moses and the convective mixing length is $0.1 \times H$. The measured parallax of 2M 0415 is 175.2 mas (Dupuy & Liu 2012) which corresponds to a distance of 5.707 pc. Combining this with the best-fit model C_k value (1.84×10^{-19}) provides a radius of 1.05 R_J for 2M 0415. The interpolated radius from the SONORA BOBCAT grid for this object is 0.98 R_J. This shows much better agreement with the calculated radius of the object compared to Gl 570D. The M-band spectrum of this best-fit model compared to the M-band data for 2M 0415 is also shown in the bottom left panel. Atmospheric properties of the best-fit model are shown in the three bottom right panels. This best-fit model has a second sandwiched radiative zone and CO, CH₄, H₂O, and HCN are quenched in this sandwiched radiative zone whereas CO₂ is quenched in the upper detached convective zone.

3.5.2. WISE 0313, UGPS 0722, WISE 2056 and WISE 1541

Miles et al. (2020) has obtained M-band observations of the late T and early Y-dwarfs WISE 0313, UGPS 0722, WISE 2056, and WISE 1541. However, these M-band spectra are not flux calibrated. Using photometry collected from various studies and the SONORA evolutionary tracks, Miles et al. (2020) found ranges of T_{eff} and $\log(g)$ values for these objects. We use our models along with these photometry datasets (see Table 2 in Miles et al. (2020) for photometry obtained from Skrutskie et al. (2006); Kirkpatrick et al. (2011); Lucas et al. (2010); Leggett et al. (2013); Schneider et al. (2015); Geballe

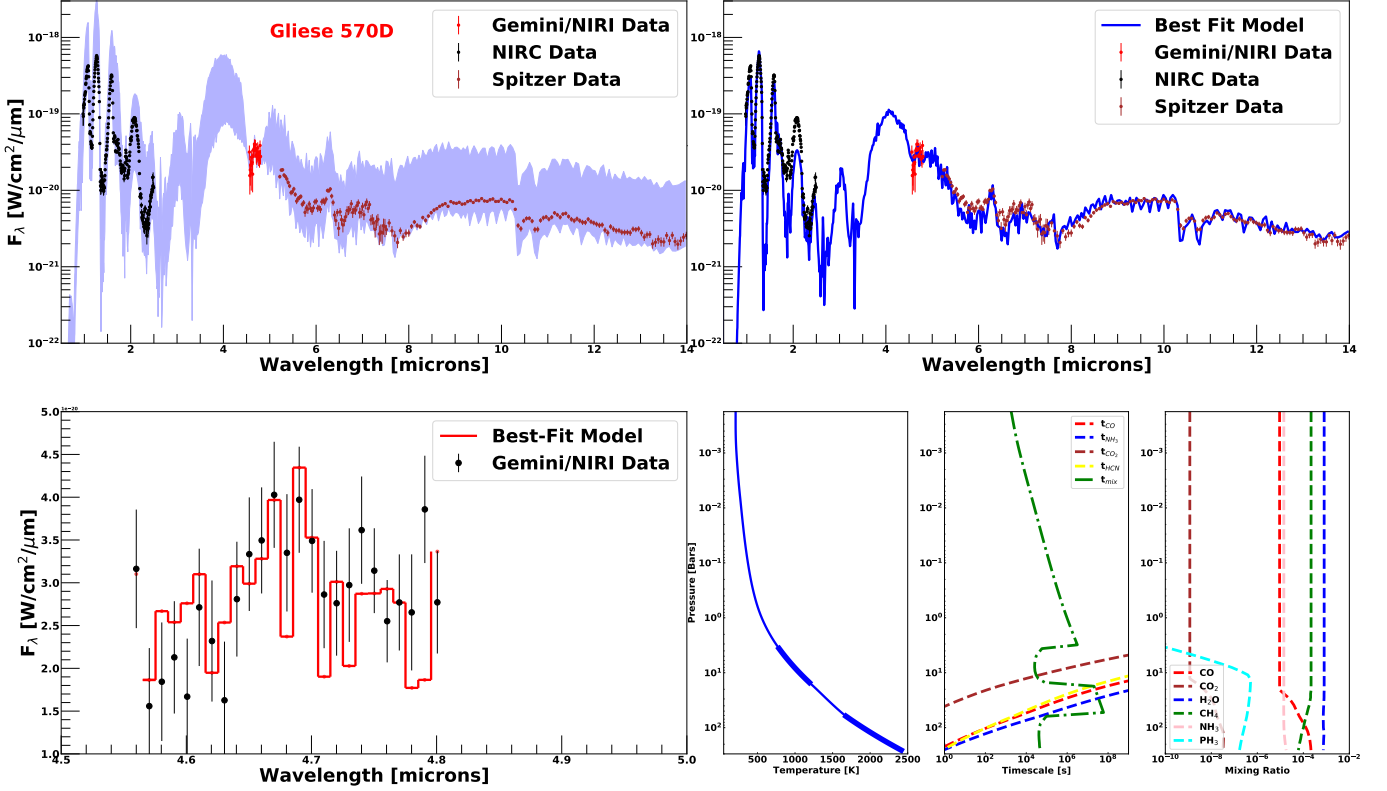


Figure 15. The **top left panel** shows the observed M-band spectra of Gl 570D with red points, the 1-2.5 μm observations of Gl 570D with black points and the *Spitzer* IRS measurements with brown points. The flux values sampled by the top 131 models with the least G_k parameter after fitting the M-band spectra only are shown with the shaded blue region. The **top right panel** shows the best-fit model obtained by fitting the M-band spectra, the 1-2.5 μm data, and the *Spitzer* 5-14 μm data for Gl 570D. The **bottom left panel** shows a comparison of the best-fit model with the M-band spectra only. The **bottom right panels** shows the $T(P)$ profile of the best fit model, the t_{mix} and t_{chem} of different quenched species as a function of pressure, and the rightmost panel shows the volume mixing ratios of CO, CH₄, NH₃, H₂O, CO₂ and PH₃.

et al. (2001); Knapp et al. (2004); Leggett et al. (2015); Golimowski et al. (2004); Leggett et al. (2017); Patten et al. (2006); Kirkpatrick et al. (2012); Cutri et al. (2021); Luhman & Esplin (2016); Schneider et al. (2016); Wright et al. (2014); Esplin et al. (2016)) to find a similar range of T_{eff} values for each of these sources. Figure 17 shows the map of χ^2 values in a T_{eff} vs. $\log(g)$ parameter space obtained by comparing our models with observed photometry of WISE 0313. It is clear that the χ^2 values are sensitive to the T_{eff} of models but there is not much sensitivity to the $\log(g)$ of the models. This method helps us in identifying a range ($\delta T = 100$ K) of T_{eff} values for each object. Then using models within this T_{eff} range we try to determine the best-fit atmospheric model by comparing our model spectra shapes with the shape of the M-band spectra of these four objects. We use the same metric G_k and C_k defined in Equations 4 and 5 for finding the best-fit models. However, as the observed spectra lacks flux calibration, the C_k now includes the α parameter as well where $1/\alpha$ represents the unknown flux calibration of the observed spectrum. For each object, we use the models within the determined T_{eff} ranges and allow all the other parameters such as $\log(g)$, radiative zone K_{zz} and mixing length L to vary while calculating the G_k and C_k values of the models using the M-band spectrum. Then the model with the least G_k value is chosen as the best-fit model for the object.

Figure 18 shows the results of this fitting exercise for all

the four objects. The four rows in Figure 18 shows the results for WISE 0313, UGPS 0722, WISE 2056, and WISE 1541, respectively. The left columns show the best-fit spectra compared with the observational data for each object. The second column from left shows the best-fit $T(P)$ profile for each object. The third column shows the best-fit mixing timescale and chemical timescale for CO as a function of pressure for these objects and the fourth columns depicts the best-fit volume mixing ratios for each object.

We find that the best-fit model describing the WISE 0313 and UGPS 0722 data have radiative zone quenching of CO/CH₄ whereas the best-fit models describing the WISE 2056 and WISE 1541 data has CO quenching in the convective zone. Table 1 shows the values of all the parameters relevant to fitting the spectral data for all of these objects. We note that the best-fit $\log(g)$ values obtained in this work are not from fitting any spectral shape/feature directly. As can be seen in Figure 5, $\log(g)$ controls the presence/absence of a sandwiched radiative zone which in turn dictates whether gases can be quenched in regions with low or high K_{zz} . These effects of $\log(g)$ on atmospheric chemistry lead to preference of certain $\log(g)$ values over others while fitting the data.

We choose our best-fit model to be the model with the least G_k value but we also find that there are quite a few models which have G_k values only differ from the minimum only by a small amount. This shows the pres-

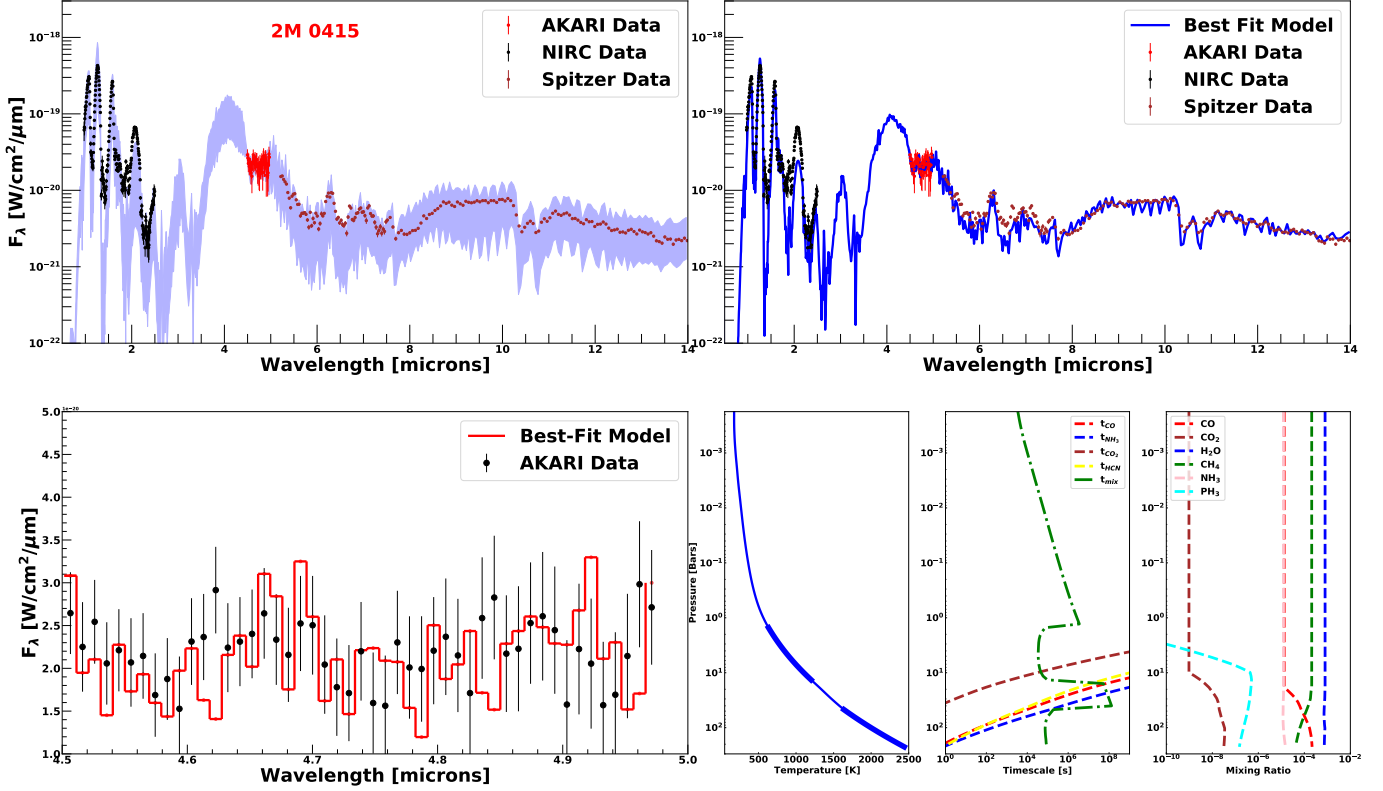


Figure 16. The **top left panel** shows the observed M-band spectra of 2M 0415 with red points, the 1-2.5 μm observations of 2M 0415 with black points and the *Spitzer* IRS measurements with brown points. The flux values sampled by the top 101 models with the least G_k parameter after fitting the M-band spectra only are shown with the shaded blue region. The **top right panel** shows the best-fit model obtained by fitting the M-band spectra, the 1-2.5 μm data and the *Spitzer* 5-14 μm data for 2M 0415. The **bottom left panel** shows a comparison of the best-fit model with the M-band spectra only. The **bottom right panels** shows the $T(P)$ profile of the best fit model, the t_{mix} and t_{chem} of different quenched species as a function of pressure, and the rightmost panel shows the volume mixing ratios of CO, CH₄, NH₃, H₂O, CO₂ and PH₃.

Source	T_{eff} Range[K]	Best-Fit T_{eff} [K]	Best-Fit $\log(g)$	Radiative K_{zz}	Convective L	M-band G_k	J-H-K+ <i>Spitzer</i> IRS G_k	C_k
Gl 570D	700–800	725	5.0	Moses	$0.1 \times H$	1.414	669.06	1.72×10^{-19}
2M 0415	600–700	675	4.75	Moses	$0.1 \times H$	0.925	514.28	1.84×10^{-19}
WISE 0313	575–675	675	4.75	Moses/100	$0.1 \times H$	3.849	–	6.477
UGPS 0722	500–600	575	4.75	Moses \times 100	$0.1 \times H$	23.884	–	11.636
WISE 2056	450–550	525	4.75	–	$0.1 \times H$	6.651	–	14.575
WISE 1541	400–450	450	4.75	–	$0.1 \times H$	5.243	–	20.275

Table 1

Results from fitting observed spectra of brown dwarfs with our model spectra. The radiative zone K_{zz} for models which do not quench at radiative zones are marked with a ‘–’ as they couldn’t be constrained.

ence of degeneracy in our models with the current precision of available data for these objects. This degeneracy will be broken with much higher precision flux calibrated M-band and shorter wavelength spectra expected from JWST which we discuss in §3.6.

3.5.3. Trends in Quench Timescales

We present the trend of the best-fit K_{zz} at P_Q for CO in these sources in Figure 19. As we mainly fit the M-band spectra of these objects in our analysis, we are only sensitive to CO and H₂O abundances and therefore we can only fit the quench K_{zz} of CO. Our best-fit quench K_{zz} for CO as a function of the best-fit T_{eff} for each object are shown with red crosses in Figure 19. The best-fit quench K_{zz} determined by Miles et al. (2020) are shown

with faded red crosses as a function of the best-fit T_{eff} obtained by Miles et al. (2020) for each object. Although the overall trend of much lower CO quench K_{zz} than the theoretical maximum in objects with T_{eff} between 600–800 K, found by Miles et al. (2020), still stands in this analysis, there are some differences in the best-fit K_{zz} and T_{eff} values between the two studies. These differences are due to multiple factors which we discuss briefly here.

Our work uses RCE models that include disequilibrium chemistry self-consistently to fit the data while equilibrium chemistry RCE models were post-processed by Miles et al. (2020) to include quenching of gases to fit the data. Figure 2 top left panel shows that including disequilibrium chemistry self-consistently can lead to large

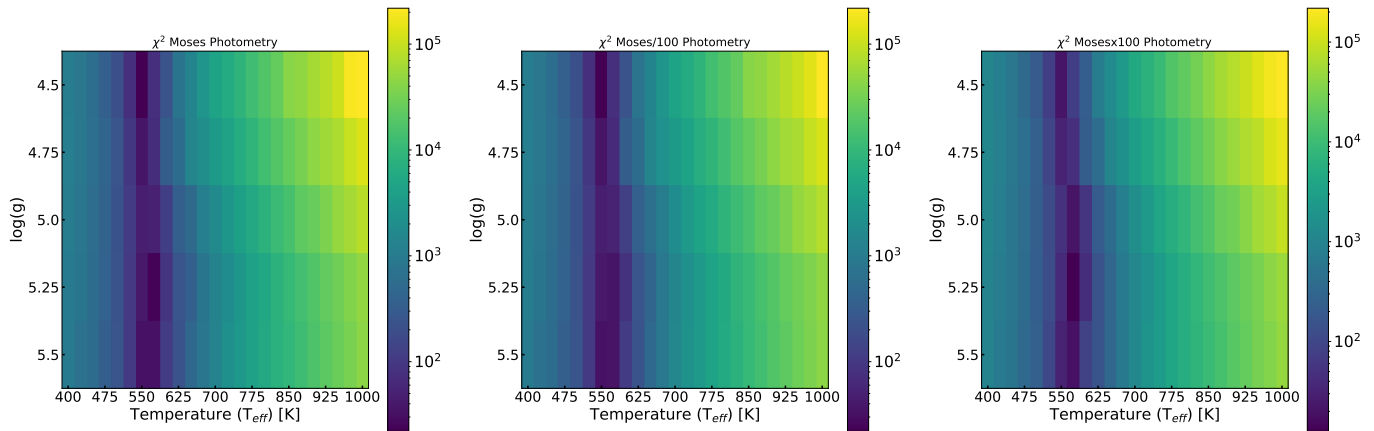


Figure 17. The left panel shows a heat map of the χ^2 value calculated using model photometry and observed photometry (Miles et al. 2020) in various infrared bands as a function of model T_{eff} and $\log(g)$ for WISE 0313. The left panel indicates models where radiative K_{zz} is fixed at Moses and the convective mixing length is H . The middle and right panels also show the χ^2 heat maps using models with radiative K_{zz} of Moses/100 and Moses \times 100, respectively. The best-fit T_{eff} is near 550 K.

changes in the $T(P)$ profile of brown dwarfs compared to equilibrium chemistry models. This can be the reason behind the ~ 50 K differences in the T_{eff} values for these objects between the two studies. For 5 of the 6 analyzed objects in this work, our assessment of CO quench K_{zz} are somewhat smaller than previously found. As some of our best-fit models have higher T_{eff} than the best-fit models of Miles et al. (2020), CO is more abundant in the deeper atmosphere of our best-fit models than those of Miles et al. (2020). Figure 2 shows that CO abundance falls very rapidly with decreasing pressure in the deep atmosphere (which is under chemical equilibrium) in these colder brown dwarfs. Therefore colder best-fit models in Miles et al. (2020) need to quench CO deeper in the atmosphere than our hotter best-fit models. So, the best-fit models presented in Miles et al. (2020) need higher CO quench K_{zz} compared to our best-fit models to produce the same CO abundance in the upper well mixed atmosphere of these brown dwarfs. Additionally, the best-fit K_{zz} presented in Miles et al. (2020) has been shown to be dependant on the gravity of the model used for fitting the data. In this work, we allowed gravity to be a free parameter while fitting the data and compared our best-fit K_{zz} in Figure 19 with the median K_{zz} obtained by Miles et al. (2020) by trying out various values of $\log(g)$.

We can use our best-fit models with CO quenching to infer the quench K_{zz} of other quenched gases like CO_2 , NH_3 or HCN in these best-fit models. The inferred quench K_{zz} values for the other gases in these objects are also shown in Figure 19. As each gas has a different t_{chem} , they also are quenched at different depths of the brown dwarf atmosphere as shown in Figure 7 and 9 for CO and CO_2 . This means that measuring the abundance of each gas can help us in measuring the height dependant K_{zz} profile in these brown dwarf atmospheres. For example, in Figure 19, the inferred quench K_{zz} for CO_2 are very different than the inferred quench K_{zz} of CO (or NH_3) as CO_2 is quenched at different pressures (having different mixing strengths) compared to CO. But inferring the height dependant K_{zz} profile of a single brown dwarf by using different gases as probes of K_{zz} at different pressures is only possible with self-consistent dise-

quilibrium chemistry models with height dependant K_{zz} profiles such as the model grid presented in this work.

The theoretical maximum limit on convective zone K_{zz} for each best-fit model is also shown with black points in Figure 19. This maximum limit on convective K_{zz} was calculated using Equation 2 with the convective heat flux fixed at σT_{eff}^4 and the mixing length L fixed at the scale height of the atmosphere. It is clear from Figure 19 that all the gases in all these objects quench at lower K_{zz} than this theoretical limit. But even though all the objects analyzed in this work have much smaller CO quench K_{zz} than the maximum convective limit shown with the black line, this does not mean that all these “quenched” occurred in the radiative zones in our models. For Gl 570D, 2M 0415, W0313, and UGPS 0722, CO is quenched in the radiative zones in our best-fit models but for W 2056 and W 1541 CO along with all the other molecules are quenched in the convective zone with a much smaller mixing length than the scale height of the atmosphere as was also suggested by the CMD analysis detailed in §3.4. Finally, we note that our best-fit models, especially for objects which lack flux-calibrated spectra, are often degenerate with the present data, and better data from observatories like JWST will be instrumental in giving us better constraints on the K_{zz} of these objects, which we discuss next.

3.6. Constraining Radiative Zone K_{zz} with JWST

An important takeaway from Miles et al. (2020) and our work is that detailed analysis of atmospheric abundances can constrain K_{zz} in brown dwarf atmospheres. There is strong evidence for mixing orders of magnitude weaker than expectations from free convection with $L = H$. The launch of JWST begs the question of whether JWST data will be able to give us better constraints on the vigor of vertical mixing in these atmospheres. We can provide a test by simulating the JWST spectra using the JWST Exposure Time Calculator (Pontoppidan et al. 2016) with some of the emission spectra from our model grid. As an illustrative example, we use the spectrum of a 700 K object. In the left panels of Figure 20 we examine three models at $\log(g)$ of 5.5, where the radiative zone K_{zz} is “Moses \times 100”, “Moses”, and “Moses/100”

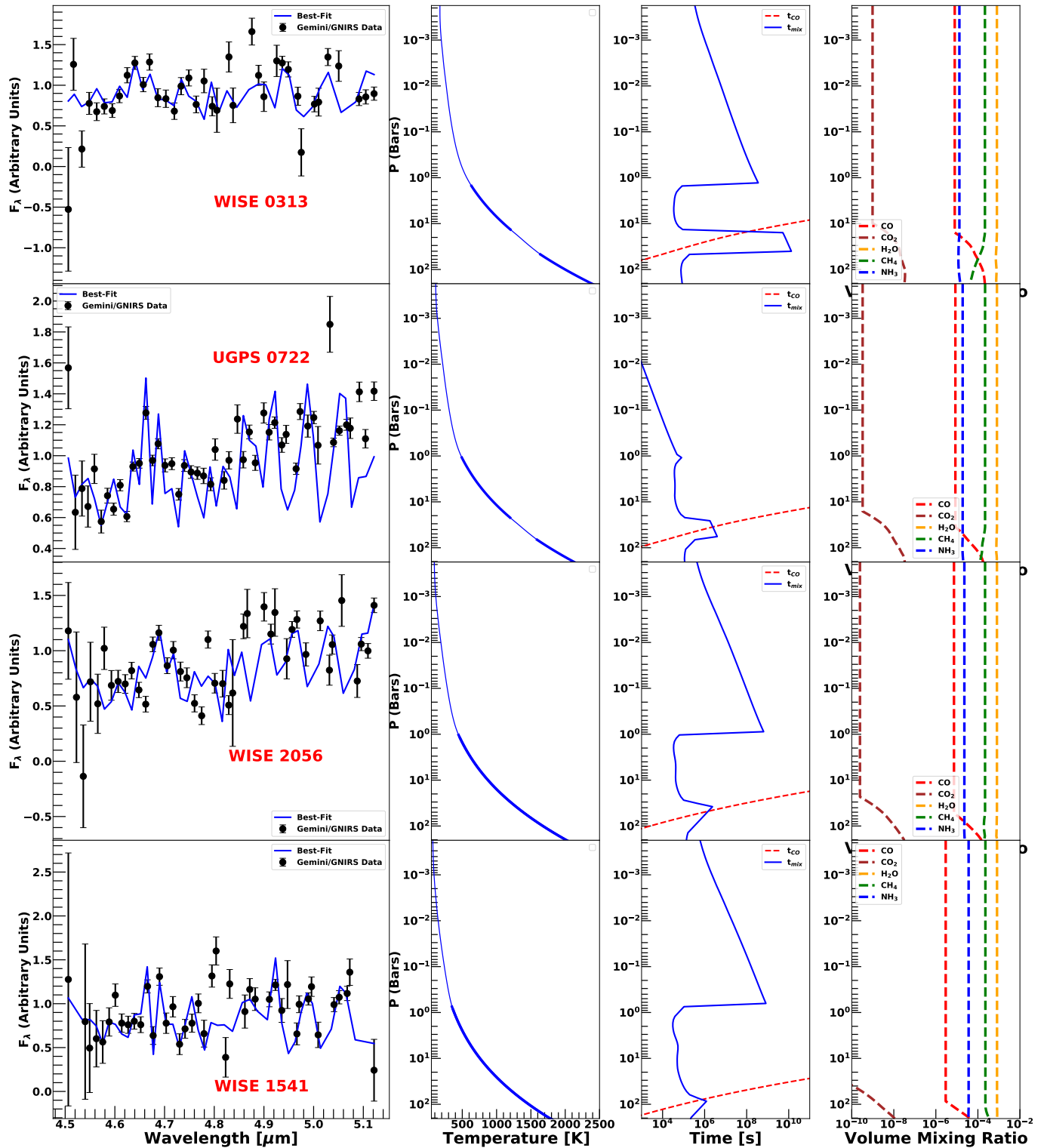


Figure 18. The best-fit atmospheric models and their comparison with data are shown in this figure. **Each row** corresponds to a different object. The **left most column** shows the best-fit M-band spectra along with the observed data from Miles et al. (2020). The **second left column** shows the best-fit $T(P)$ profile for these objects from the grid of models presented in this paper. The **third column** shows the best-fit mixing timescale in blue along with the chemical timescale for CO in red as a function of pressure. The volume mixing ratios of various atmospheric gases are shown in the **fourth column** for each object.

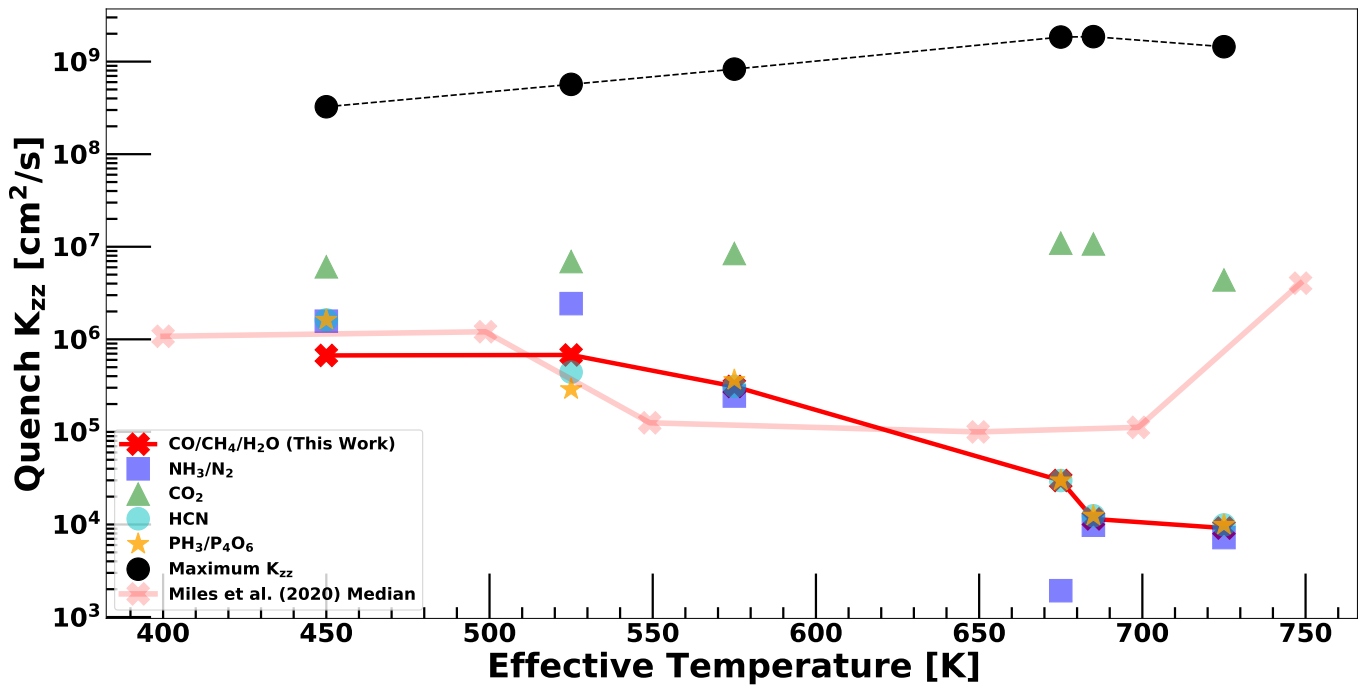


Figure 19. The best fit quench K_{zz} of CO for each object is shown as a function of their best-fit T_{eff} with the red crosses. The median best-fit quench K_{zz} vs. T_{eff} inferred by Miles et al. (2020) with lower gravity models are shown with the faded red crosses. The inferred quench K_{zz} for NH_3 , CO_2 , HCN , and PH_3 from the best-fit models for each object are also shown as a function of their best-fit T_{eff} . The black points show the theoretically maximum K_{zz} allowed from mixing length theory for these best-fit models.

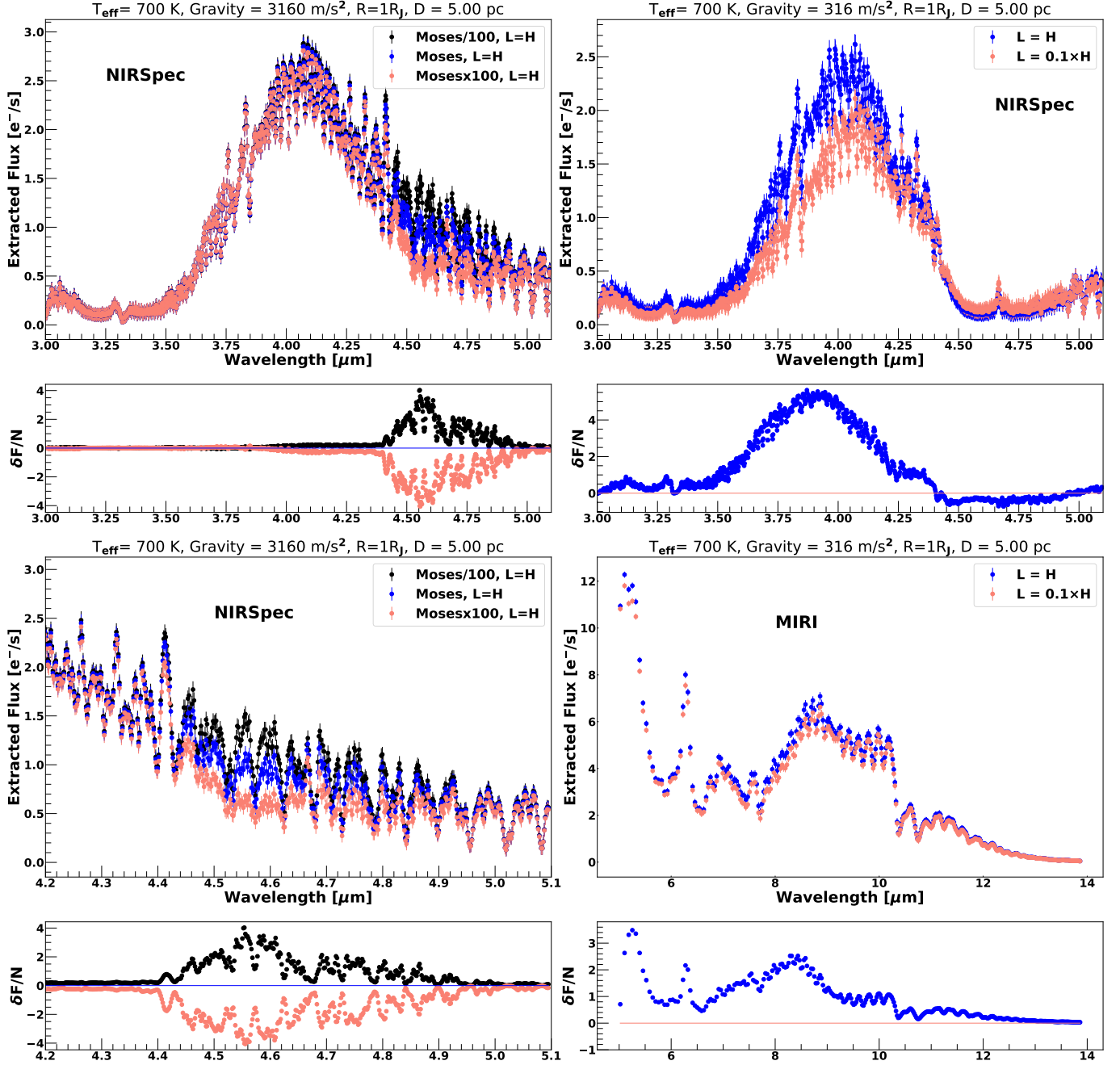


Figure 20. Simulated data from JWST instruments are shown for one of our model brown dwarfs with T_{eff} of 700 K. The three colors in the simulated data correspond to models with different radiative zone K_{zz} . The **top left panel** shows the simulated NIRSpec spectra of a $\log(g)=5.5$ object with an exposure time of 10 minutes while the **bottom left panel** shows a zoomed version of the top left panel to emphasize how JWST NIRSpec M-band observations can clearly distinguish between different K_{zz} in the radiative zones for these T-dwarfs. The **top right panel** shows the NIRSpec simulated data for a brown dwarf with T_{eff} of 700 K and $\log(g)$ of 4.5. The two colors represent different K_{zz} in the convective zone but the same K_{zz} in the radiative zone. The **bottom right panel** shows MIRI LRS simulated data for the same models shown in the top right panels. To compare the differences between the simulated data from different models to the typical JWST noise, the ratio of the flux differences (δF) between various models and the simulated JWST noise (N) is shown below each of these panels. This shows that both convective and radiative zone K_{zz} can be constrained with JWST.

and $L = H$. We assume that the source has a radius of $1R_J$ and is at a distance of 5 pc. The temperature and distance chosen for this exercise are somewhat representative of objects like Gl 570D and 2M 0415.

The NIRSpec panels (which is 3 of the 4 figures) assume fixed slit mode with the G395M grating and the F290LP filter for these simulations. The results are impressive, with only a total of 10.39 minutes exposure time, simulated with 10 groups per integration, 2 integration per exposure, and 5 exposures. It is clear from the top left panel that the radiative zone K_{zz} can be constrained with high precision with about a total ~ 10 minutes exposure time per object in this JWST observing mode. This time includes all the 5 exposures used for this simulation. In order to emphasize the difference arising in the synthetic counts from the three models in the 4.5–5 μm range, the bottom left panel shows a zoomed in view of the 4.3–5 μm wavelength range, focusing on CO absorption, where the main sensitivity of the data to radiative zone K_{zz} lies. The top right panel shows a lower-gravity model ($\log(g)=4.5$), where a lower pressure photosphere favors CO at the expense of CH_4 . Here the blue model is simulated from a model where the convective mixing length $L = H$ whereas the salmon colored data is simulated from a model where the convective mixing length is $L = 0.1 \times H$. The radiative zone K_{zz} of both the cases in this panel are “Moses $\times 100$ ”. Both of these models have the quenching of all relevant gases occurring in the convective zone. The large differences in the synthetic counts between the two models in the 3.5–4.25 μm range shows that JWST data can also be used to probe differences in the convective zone K_{zz} with exposure times of ~ 10 minutes.

Radiative and convective zone K_{zz} can be probed with other wavelengths as well. The bottom right panel in Figure 20 shows the simulated spectrum of the two cases shown in the top right panel but when observed by the MIRI instrument. The MIRI LRS mode was used for this data simulation along with a 60 minutes exposure time. Differences between the two model spectra arise between 5–9 μm . A comparison with Figure 1 shows that these differences mainly arise from different CH_4 , H_2O and NH_3 abundances due to differences in the convective zone K_{zz} .

4. DISCUSSION

4.1. PH_3 Quenching

Under chemical equilibrium conditions the major phosphorus-bearing molecule PH_3 is expected to be removed by oxidation at low temperatures in the visible atmospheres of giant planets and colder brown dwarfs. A number of oxidation products have been considered (see Visscher 2020), including P_4O_6 (e.g., Fegley & Lodders 1994; Visscher et al. 2006), P_4O_{10} (Borunov et al. 1995), H_3PO_4 (Wang et al. 2016), or condensation of $\text{NH}_4\text{H}_2\text{PO}_4$ (Fegley & Lodders 1994; Visscher et al. 2006; Morley et al. 2018). Following the work of Visscher & Fegley (2005); Visscher et al. (2006); Miles et al. (2020), as a representative example of PH_3 oxidation we may consider the conversion of PH_3 into P_4O_6 via the net thermochemical reaction,

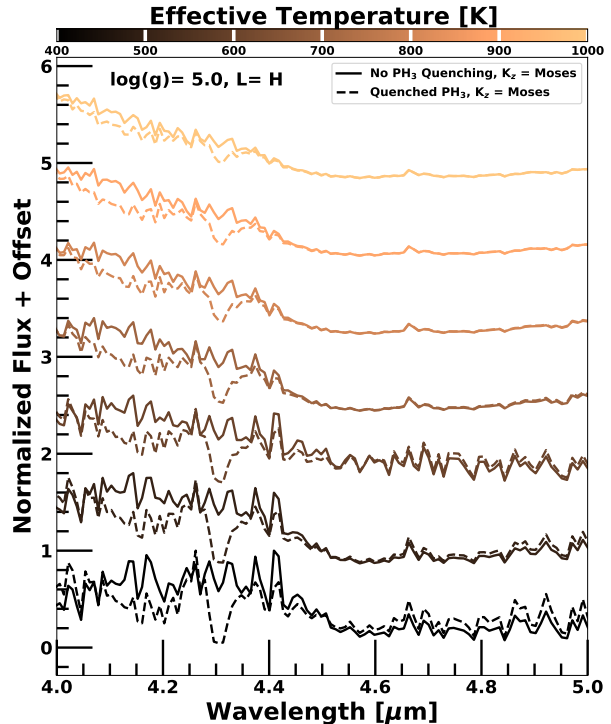
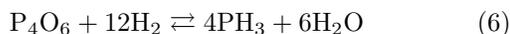


Figure 21. Effect of PH_3 quenching on the spectrum has been shown by comparing them with disequilibrium chemistry model spectra where PH_3 is not quenched. Models with different T_{eff} values ranging from 400 K to 1000 K, with a step of 100 K, are shown from bottom to top. All of these models have $\log(g)=5$.

However, the t_{chem} of $\text{PH}_3 \rightarrow \text{P}_4\text{O}_6$ is such that it can be quenched in the deeper atmosphere, leading to a large enhancement of PH_3 in the photosphere. This effect makes PH_3 the major phosphorus bearing gas in atmospheres of Jupiter and Saturn (Lodders 2004; Visscher & Fegley 2005). PH_3 is expected to be found in colder brown dwarfs as well (Visscher et al. 2006; Morley et al. 2018).

Due to expected small affect of P-bearing molecules on brown dwarf temperature structures, we did not include PH_3 as a molecule to be mixed on-the-fly for converging to a final atmospheric state. However, in order to test the effect of PH_3 on the emergent thermal emission spectra, we post-process our converged disequilibrium chemistry model with quenched PH_3 abundance. The t_{chem} for $\text{PH}_3 \rightarrow \text{P}_4\text{O}_6$ is given by Visscher & Fegley (2005),

$$t_{\text{chem}} = \frac{1.9 \times 10^{12}}{[\text{OH}]} \exp\left(\frac{6013.6}{T}\right) \text{ s} \quad (7)$$

where $[\text{OH}]$ represents the number density of OH molecules in units of cm^{-3} . With our converged disequilibrium chemistry modules, we calculate the mixing ratio of OH molecules using Visscher & Fegley (2005),

$$X_{\text{OH}} = \frac{K X_{\text{H}_2\text{O}} \sqrt{X_{\text{H}_2}}}{\sqrt{P}} \quad (8)$$

where X_{OH} , $X_{\text{H}_2\text{O}}$, and X_{H_2} represent the volume mixing ratios of each of these components and P represents the pressure in bars. The constant K is temperature dependant and based on fits to thermodynamic data, and is given by,

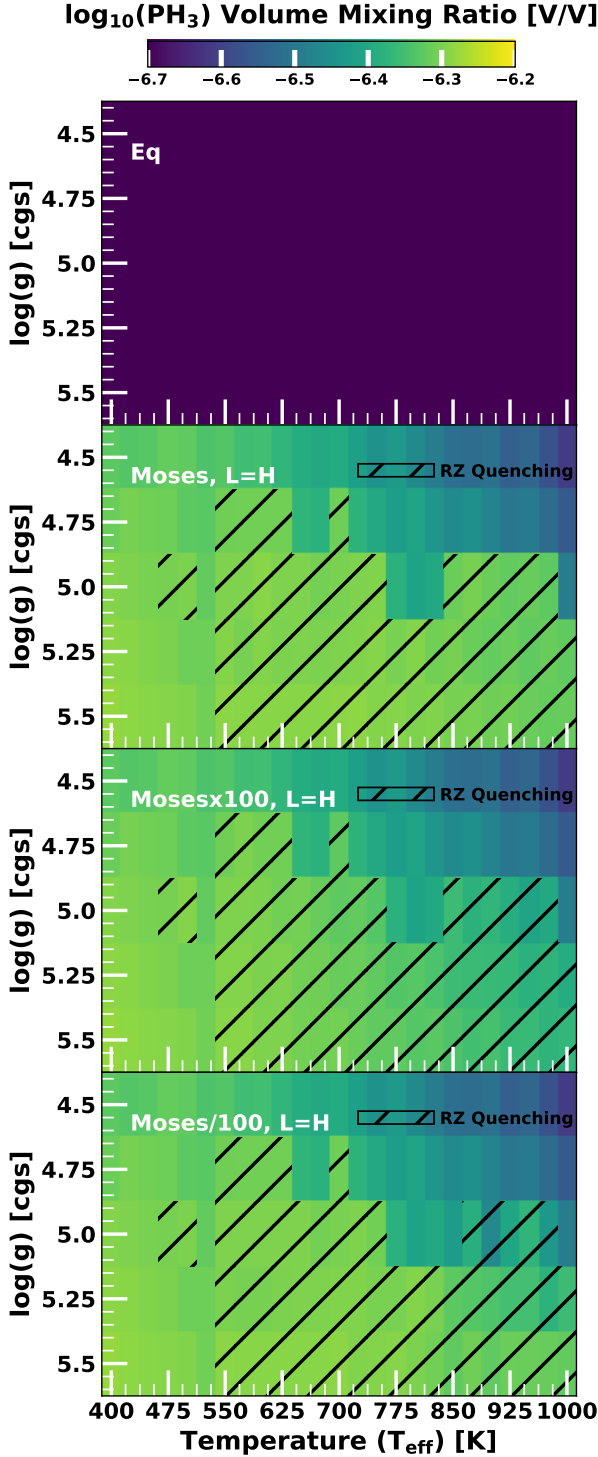


Figure 22. Top panel shows the equilibrium chemistry abundance of PH_3 at pressures where $T(P) = T_{\text{eff}}$ in our T_{eff} vs. gravity grid of chemical equilibrium models. The **second, third and last panels** depict PH_3 abundance within the T_{eff} vs. gravity parameter space in our disequilibrium chemistry models. The second, third and last panels correspond models with radiative zone K_{zz} values of “Moses”, “Moses \times 100”, and “Moses/100”, respectively while the convective zone mixing length L was fixed at the scale height H . Models where PH_3 was quenched in a radiative zone are marked with black hatches. PH_3 was quenched at a convective zone in the rest of the models.

$$K = 3.672 - \frac{14791}{T} \quad (9)$$

where T is the temperature in K. Using Equations 7, 8, and 9 we determine the t_{chem} of PH_3 for all our converged models. Then using our converged t_{mix} profiles we determine P_Q for PH_3 and quench it creating another set of our models which has quenched PH_3 abundances. Using these modified chemical compositions, we create another set of thermal emission spectra models with quenched PH_3 abundances. Figure 21 compares the differences in spectra caused by the quenching of PH_3 with disequilibrium models where PH_3 is not quenched. This quenching of PH_3 increases the PH_3 volume mixing ratios dramatically, from $\leq 10^{-30}$ under chemical equilibrium, to $\sim 10^{-6}$ to 10^{-7} due to quenching. The main impact of this increase appears between 4-4.5 μm in the thermal emission spectrum as shown in Figure 21. This also suggests that PH_3 may become an important enough atmospheric opacity source to have a small effect on their $T(P)$ profiles as well, which we will aim to explore in future work.

Figure 22 shows the parameter space of models where PH_3 quenches at the radiative zone and convective zones for different levels of radiative zone K_{zz} when the convective mixing length is H . This also shows that depending on the properties of the object in question, PH_3 can also be used as a probe for determining radiative or convective zone K_{zz} . The region around 4.0-4.4 μm is difficult to probe from the ground (Miles et al. 2020), but it is clear from Figure 21 that these PH_3 should be readily detectable with *JWST*. Interestingly, Morley et al. (2018) didn’t detect PH_3 between 4.0-4.4 μm in WISE 0855 even though it is expected to be present in it’s atmosphere theoretically. Determining the strength of these features, or their absence, will have important implications in understanding K_{zz} and phosphorus chemistry.

4.2. Clouds

The models presented in this work are cloud-free. However, H_2O condensation in the upper atmospheres of objects can begin at $T_{\text{eff}} \leq 450$ K (Morley et al. 2014) and these clouds can start becoming an important opacity source colder than ~ 400 K (Morley et al. 2014). Once water clouds become optically thick, they can change the overall energy balance of the atmosphere impacting the $T(P)$ profile. The presence of disequilibrium chemistry causes a cooling down of the upper atmosphere, compared to equilibrium chemistry, but the opacity of clouds has the opposite effect of heating up the $T(P)$ profile.

Importantly, the cloud particle size and vertical extent are also quite sensitive to the mixing parameter K_{zz} as mixing helps to keep cloud particles aloft against their gravitational settling (Ackerman & Marley 2001b). Cloud particle sizes are an extremely important parameter in dictating their scattering properties (Mukherjee et al. 2021; Ackerman & Marley 2001b) and hence K_{zz} has a large effect on the cloud opacities in these atmospheres. Therefore, it is clear that information gleaned on K_{zz} from disequilibrium chemistry studies will be important in improving cloud models. Future studies should aim for a self-consistent treatment of disequilibrium chemistry and cloud formation with a self-consistent treatment of K_{zz} within a given model atmo-

sphere. Recently, [Mang et al. \(2022\)](#) showed that water clouds have a large impact on the M-band spectra of colder Y-dwarfs, with $T_{\text{eff}} \leq 400$ K, just below the lower T edge of our study. Somewhat different than this work, [Mang et al. \(2022\)](#) calculated the radiative zone K_{zz} , needed for cloud modeling, by setting the mixing length to one-tenth of the scale height in the radiative zones. This approach also leads to smaller K_{zz} in the radiative zones compared to the convective zones. When we extend our disequilibrium chemistry model to colder objects, inclusion of clouds in this framework is an important milestone.

5. SUMMARY AND CONCLUSION

In this work, we have used a newly developed Python-based 1D radiative-convective equilibrium model with the capability to self-consistently capture disequilibrium chemistry in brown dwarf and exoplanet atmospheres. Using this model we have created a self-consistent grid of brown dwarf models between T_{eff} of 400-1000 K with an increment of 25 K and $\log(g)$ of 4.5-5.5 with an increment of 0.25. Instead of using a constant K_{zz} prescription throughout the entire atmosphere as done in earlier work (e.g. [Karalidi et al. 2021](#); [Phillips et al. 2020](#)) or self-consistent K_{zz} in the convective zones and constant K_{zz} in the radiative zones (e.g. [Hubeny & Burrows 2007](#)), we use a self-consistent $T(P)$ structure dependant K_{zz} profile for the entire atmosphere for our grid. In the convective zone, we use mixing length theory with two different mixing lengths whereas in the radiative zones we use various multiples of a T and P -dependent K_{zz} prescription. The idea behind these models was to assess whether disequilibrium chemical abundance can be used as a probe for temperature structure and mixing processes below the visible atmosphere in brown dwarfs. With this grid in hand, we conclude on the following points.

1. As found by others, a self-consistent treatment of disequilibrium chemistry causes cooling of $T(P)$ profiles, especially in the upper atmospheres of late T and early Y-dwarfs.
2. Post-processing equilibrium chemistry models by quenching various molecules instead of using self-consistent models with disequilibrium chemistry should be avoided because this can lead to significant errors in the calculated abundances of molecules like CO, CH₄ and NH₃. This can also lead to incorrect $T(P)$ profiles. Both of these results are especially relevant in the JWST era with significantly higher S/N mid-infrared data.
3. Self-consistent models including disequilibrium chemistry also show a large change in the location, depths, and number of radiative and convective zones in brown dwarfs compared to self-consistent models with equilibrium chemistry.
4. Depending on the strengths of radiative zone K_{zz} and convective mixing length, gases like CO, CH₄, NH₃, CO₂ and PH₃ can be quenched in the radiative zones of brown dwarfs in a large fraction of the T_{eff} and $\log(g)$ parameter space.

5. Since different molecules have different t_{chem} values, which leads them to quench at different pressure levels. This means that some molecules may quench in radiative zones, while other may quench in convective zones, in the same atmosphere, such that different molecules may be quenched by very different K_{zz} values.
6. The M-band thermal spectra of objects where radiative zone quenching occurs, is very sensitive to the K_{zz} in the radiative zones. This can lead to non-monotonic behavior in the CO abundance and spectra as a function of T_{eff} . This is especially exciting because it provides an avenue to observationally constrain the highly uncertain radiative zone K_{zz} in these objects.
7. The mid-infrared photometric bands – MKO L' and MKO M, and WISE 1 and 2, are quite sensitive to the K_{zz} in the radiative zone. We also find that our models provide a better fit to the infrared photometry of these objects than chemical equilibrium models.
8. We use our models to fit the M-band spectra of 6 brown dwarfs – Gliese 570 D, 2MASS J0415-0935, WISE 0313, UGPS 0722, WISE 2056, and WISE 1541. We determine the best-fit atmospheric state for these objects including the quench level K_{zz} of quenched gases in these objects. Similar to [Miles et al. \(2020\)](#), we also find that these objects have K_{zz} much smaller than the theoretical convective mixing limit. We also see that the best fit quench K_{zz} in these objects are very low between T_{eff} of 675-800 K while it shows an increase with lowering T_{eff} for objects with T_{eff} below 575 K.
9. By performing some signal-to-noise calculations for JWST, we conclude that short exposure time observations can provide us with excellent measurements of the radiative and convective zone K_{zz} in brown dwarfs.
10. We also expect JWST to find clearly detectable disequilibrium PH₃ abundances in the atmospheres of these objects.

The non-monotonic behaviour of atmospheric chemistry, as a function of T_{eff} and $\log(g)$, found in this work indicates the need to explore these effects with even finer grid spacing than this work in parameters like T_{eff} (25 K in this work), $\log(g)$ (0.25 dex in this work), and K_{zz} (factor of 100 in this work). This remains the focus of a future model grid release. The model presented in this work will be updated to include self-consistent clouds in the near future. Additional future work will couple the code to the chemical kinetics model VULCAN ([Tsai et al. 2017, 2021](#)) which would enable a more rigorous self-consistent treatment of disequilibrium chemistry in our models. This will also allow us to include effects like the feedback of the disequilibrium abundances of gases like CH₄ on the entire chemical network of the atmosphere within our models, self-consistently. This will also allow us to explore the empirical trends we find in this work,

like probable slower convective mixing than typically calculated assuming free convection, more robustly. Moreover, such a coupling opens up the possibility to explore both photochemistry and vertical mixing together self-consistently, which is more relevant for irradiated exoplanets. This updated model will then be used to explore effects of vertical mixing and photochemistry for warm transiting giant planets and find additional observables to constrain K_{zz} in such planets, an important comparison sample to the non-irradiated objects explored here.

6. ACKNOWLEDGMENTS

SM thanks the UC Regents Fellowship award for supporting him for this work. JFF acknowledges the support of NASA XRP grant 80NSSC19K0446. We acknowledge use of the lux supercomputer at UC Santa Cruz, funded by NSF MRI grant AST 1828315. SM also thanks Caroline Morley for very useful inputs for preparing the color-magnitude diagrams presented here. We thank the anonymous referee for very insightful comments which helped in the betterment of this manuscript.

Software: PICASO 3.0 (Mukherjee et al. 2022), PICASO (Batalha et al. 2019), pandas (McKinney 2010), NumPy (Walt et al. 2011), IPython (Pérez & Granger 2007), Jupyter (Kluyver et al. 2016), matplotlib (Hunter 2007), the model grid will be formally released via Zenodo.

REFERENCES

- Ackerman, A. S., & Marley, M. S. 2001a, *ApJ*, 556, 872
 —, 2001b, *ApJ*, 556, 872
 Allard, F., Homeier, D., & Freytag, B. 2012, *Philosophical Transactions of the Royal Society of London Series A*, 370, 2765
 Allen, M., Yung, Y. L., & Waters, J. W. 1981, *Journal of Geophysical Research: Space Physics*, 86, 3617
 Amundsen, D. S., Tremblin, P., Manners, J., Baraffe, I., & Mayne, N. J. 2017, *A&A*, 598, A97
 Batalha, N. E., Marley, M. S., Lewis, N. K., & Fortney, J. J. 2019, *ApJ*, 878, 70
 Beer, R. 1975, *ApJL*, 200, L167
 Bordwell, B., Brown, B. P., & Oishi, J. S. 2018, *ApJ*, 854, 8
 Borunov, S., Dorofeeva, V., Khodakovskiy, I., et al. 1995, *Icarus*, 113, 460
 Burgasser, A. J., Geballe, T. R., Leggett, S. K., Kirkpatrick, J. D., & Golimowski, D. A. 2006, *ApJ*, 637, 1067
 Burgasser, A. J., Kirkpatrick, J. D., Cutri, R. M., et al. 2000, *ApJL*, 531, L57
 Burgasser, A. J., Kirkpatrick, J. D., Brown, M. E., et al. 2002, *ApJ*, 564, 421
 Burrows, A., Sudarsky, D., & Lunine, J. I. 2003, *The Astrophysical Journal*, 596, 587
 Burrows, A., Marley, M., Hubbard, W. B., et al. 1997, *ApJ*, 491, 856
 Bézard, B., Lellouch, E., Strobel, D., Maillard, J.-P., & Drossart, P. 2002, *Icarus*, 159, 95
 Cushing, M. C., Marley, M. S., Saumon, D., et al. 2008, *ApJ*, 678, 1372
 Cushing, M. C., Kirkpatrick, J. D., Gelino, C. R., et al. 2011, *ApJ*, 743, 50
 Cushing, M. C., Hardegree-Ullman, K. K., Trucks, J. L., et al. 2016, *ApJ*, 823, 152
 Cutri, R. M., Wright, E. L., Conrow, T., et al. 2021, *VizieR Online Data Catalog*, II/328
 Dupuy, T. J., & Kraus, A. L. 2013, *Science*, 341, 1492
 Dupuy, T. J., & Liu, M. C. 2012, *ApJS*, 201, 19
 Esplin, T. L., Luhman, K. L., Cushing, M. C., et al. 2016, *ApJ*, 832, 58
 Fegley, Jr., B., & Lodders, K. 1994, *Icarus*, 110, 117
 Fegley, B., J., & Prinn, R. G. 1985, *ApJ*, 299, 1067
 Fegley, Bruce, J., & Lodders, K. 1996, *ApJL*, 472, L37
 Fortney, J. J., Lodders, K., Marley, M. S., & Freedman, R. S. 2008, *ApJ*, 678, 1419
 Fortney, J. J., Marley, M. S., & Barnes, J. W. 2007, *ApJ*, 659, 1661
 Fortney, J. J., Marley, M. S., Lodders, K., Saumon, D., & Freedman, R. 2005, *ApJL*, 627, L69
 Fortney, J. J., Visscher, C., Marley, M. S., et al. 2020, *AJ*, 160, 288
 Freytag, B., Allard, F., Ludwig, H. G., Homeier, D., & Steffen, M. 2010, *A&A*, 513, A19
 Gandhi, S., & Madhusudhan, N. 2017, *MNRAS*, 472, 2334
 Gao, P., Thorngren, D. P., Lee, G. K. H., et al. 2020, *Nature Astronomy*, doi:10.1038/s41550-020-1114-3
 Gardner, J. P., Mather, J. C., Clampin, M., et al. 2006, *Space Sci. Rev.*, 123, 485
 Geballe, T. R., Saumon, D., Golimowski, D. A., et al. 2009, *ApJ*, 695, 844
 Geballe, T. R., Saumon, D., Leggett, S. K., et al. 2001, *ApJ*, 556, 373
 Gierasch, P. J., & Conrath, B. J. 1985, in *Recent Advances in Planetary Meteorology*, ed. G. E. Hunt, 121–146
 Golimowski, D. A., Leggett, S. K., Marley, M. S., et al. 2004, *AJ*, 127, 3516
 Hubeny, I., & Burrows, A. 2007, *ApJ*, 659, 1458
 Hunter, J. D. 2007, *Computing in Science & Engineering*, 9, 90
 Karalidi, T., Apai, D., Schneider, G., Hanson, J. R., & Pasachoff, J. M. 2015, *ApJ*, 814, 65
 Karalidi, T., Marley, M., Fortney, J. J., et al. 2021, *ApJ*, 923, 269
 Kirkpatrick, J. D., Cushing, M. C., Gelino, C. R., et al. 2011, *ApJS*, 197, 19
 Kirkpatrick, J. D., Gelino, C. R., Cushing, M. C., et al. 2012, *ApJ*, 753, 156
 Kluyver, T., Ragan-Kelley, B., Pérez, F., et al. 2016, in *ELPUB*, 87–90
 Knapp, G. R., Leggett, S. K., Fan, X., et al. 2004, *AJ*, 127, 3553
 Komacek, T. D., Showman, A. P., & Parmentier, V. 2019, *The Astrophysical Journal*, 881, 152
 Larson, H. P., Fink, U., & Treffers, R. C. 1978, *ApJ*, 219, 1084
 Larson, H. P., Treffers, R. R., & Fink, U. 1977, *ApJ*, 211, 972
 Lee, E. K. H., Parmentier, V., Hammond, M., et al. 2021, *Monthly Notices of the Royal Astronomical Society*, 506, 2695
 Leggett, S. K., Morley, C. V., Marley, M. S., & Saumon, D. 2015, *ApJ*, 799, 37
 Leggett, S. K., Morley, C. V., Marley, M. S., et al. 2013, *ApJ*, 763, 130
 Leggett, S. K., Tremblin, P., Esplin, T. L., Luhman, K. L., & Morley, C. V. 2017, *ApJ*, 842, 118
 Leggett, S. K., Saumon, D., Marley, M. S., et al. 2012, *ApJ*, 748, 74
 Liu, M. C., Dupuy, T. J., & Allers, K. N. 2016, *ApJ*, 833, 96
 Lodders, K. 2004, *ApJ*, 611, 587
 Lucas, P. W., Tinney, C. G., Burningham, B., et al. 2010, *MNRAS*, 408, L56
 Luhman, K. L., & Esplin, T. L. 2016, *AJ*, 152, 78
 Malik, M., Grosheintz, L., Mendonça, J. M., et al. 2017, *AJ*, 153, 56
 Mang, J., Gao, P., Hood, C. E., et al. 2022, *arXiv e-prints*, arXiv:2202.01355
 Marley, M., Saumon, D., Morley, C., et al. 2021, *Sonora Bobcat: cloud-free, substellar atmosphere models, spectra, photometry, evolution, and chemistry*, doi:10.5281/zenodo.5063476
 Marley, M. S., & McKay, C. P. 1999, *Icarus*, 138, 268
 Marley, M. S., & Robinson, T. D. 2015, *ARA&A*, 53, 279
 Marley, M. S., Saumon, D., Cushing, M., et al. 2012, *The Astrophysical Journal*, 754, 135
 Marley, M. S., Saumon, D., Guillot, T., et al. 1996, *Science*, 272, 1919
 Marley, M. S., Saumon, D., Visscher, C., et al. 2021, *ApJ*, 920, 85
 McKinney, W. 2010, in *Proceedings of the 9th Python in Science Conference*, ed. S. van der Walt & J. Millman, 51 – 56
 Metchev, S. A., Heinze, A., Apai, D., et al. 2015, *ApJ*, 799, 154
 Miles, B. E., Skemer, A. J. I., Morley, C. V., et al. 2020, *AJ*, 160, 63
 Morley, C. V., Marley, M. S., Fortney, J. J., et al. 2014, *ApJ*, 787, 78
 Morley, C. V., Skemer, A. J., Allers, K. N., et al. 2018, *ApJ*, 858, 97
 Moses, J. I., Fouchet, T., Bézard, B., et al. 2005, *Journal of Geophysical Research (Planets)*, 110, E08001
 Moses, J. I., Tremblin, P., Venot, O., & Miguel, Y. 2021, *Experimental Astronomy*, arXiv:2103.07023
 Moses, J. I., Visscher, C., Fortney, J. J., et al. 2011, *ApJ*, 737, 15
 Mukherjee, S., Batalha, N. E., Fortney, J. J., & Marley, M. S. 2022, *arXiv e-prints*, arXiv:2208.07836
 Mukherjee, S., Fortney, J. J., Jensen-Clem, R., et al. 2021, *ApJ*, 923, 113
 Noll, K. S., Geballe, T. R., & Marley, M. S. 1997, *ApJL*, 489, L87
 Oppenheimer, B. R., Kulkarni, S. R., Matthews, K., & van Kerkwijk, M. H. 1998, *ApJ*, 502, 932
 Parmentier, V., Showman, A. P., & Lian, Y. 2013, *A&A*, 558, A91
 Patten, B. M., Stauffer, J. R., Burrows, A., et al. 2006, *ApJ*, 651, 502

- Pérez, F., & Granger, B. E. 2007, *Computing in Science & Engineering*, 9
- Phillips, M. W., Tremblin, P., Baraffe, I., et al. 2020, *A&A*, 637, A38
- Pontoppidan, K., Blome, C., Braun, H., et al. 2022, arXiv e-prints, arXiv:2207.13067
- Pontoppidan, K. M., Pickering, T. E., Laidler, V. G., et al. 2016, in *Observatory Operations: Strategies, Processes, and Systems VI*, ed. A. B. Peck, R. L. Seaman, & C. R. Benn, Vol. 9910, International Society for Optics and Photonics (SPIE), 381 – 395
- Prinn, R. G., & Barshay, S. S. 1977, *Science*, 198, 1031
- Saumon, D., Marley, M. S., & Lodders, K. 2003, arXiv e-prints, astro
- Schneider, A. C., Cushing, M. C., Kirkpatrick, J. D., & Gelino, C. R. 2016, *ApJL*, 823, L35
- Schneider, A. C., Cushing, M. C., Kirkpatrick, J. D., et al. 2015, *ApJ*, 804, 92
- Showman, A. P., Fortney, J. J., Lian, Y., et al. 2009, *ApJ*, 699, 564
- Skrutskie, M. F., Cutri, R. M., Stiening, R., et al. 2006, *AJ*, 131, 1163
- Smith, M. D. 1998, *Icarus*, 132, 176
- Sorahana, S., & Yamamura, I. 2012, *The Astrophysical Journal*, 760, 151
- Suárez, G., & Metchev, S. 2022, arXiv e-prints, arXiv:2205.00168
- Tan, X. 2022, *Monthly Notices of the Royal Astronomical Society*, 511, 4861
- Tan, X., & Showman, A. P. 2021, *MNRAS*, 502, 2198
- Tsai, S.-M., Lyons, J. R., Grosheintz, L., et al. 2017, *ApJS*, 228, 20
- Tsai, S.-M., Malik, M., Kitzmann, D., et al. 2021, *ApJ*, 923, 264
- Visscher, C. 2020, *Journal of Geophysical Research (Planets)*, 125, e06526
- Visscher, C., & Fegley, Bruce, J. 2005, *ApJ*, 623, 1221
- Visscher, C., Lodders, K., & Fegley, Jr., B. 2010a, *ApJ*, 716, 1060
- Visscher, C., Lodders, K., & Fegley, Bruce, J. 2006, *ApJ*, 648, 1181
- Visscher, C., & Moses, J. I. 2011, *ApJ*, 738, 72
- Visscher, C., Moses, J. I., & Saslow, S. A. 2010b, *Icarus*, 209, 602
- Vos, J. M., Faherty, J. K., Gagné, J., et al. 2022, *ApJ*, 924, 68
- Walt, S. v. d., Colbert, S. C., & Varoquaux, G. 2011, *Computing in Science & Engineering*, 13, 22
- Wang, D., Gierasch, P. J., Lunine, J. I., & Mousis, O. 2015, *Icarus*, 250, 154
- Wang, D., Lunine, J. I., & Mousis, O. 2016, *Icarus*, 276, 21
- Wright, E. L., Mainzer, A., Kirkpatrick, J. D., et al. 2014, *AJ*, 148, 82
- Zahnle, K. J., & Marley, M. S. 2014, *ApJ*, 797, 41
- Zhang, X., & Showman, A. P. 2018, *ApJ*, 866, 1